The impact of helium reionization on the structure of the intergalactic medium

Monthly Notices
of the
ROYAL ASTRONOMICAL SOCIETY

Mon. Not. R. Astron. Soc. **423,** 7–25 (2012) doi:10.1111/j.1365-2966.2011.20380.x

The impact of helium reionization on the structure of the intergalactic medium

Avery Meiksin★ and Eric R. Tittley

SUPA†, Institute for Astronomy, University of Edinburgh, Blackford Hill, Edinburgh EH9 3HJ

Accepted 2011 December 12. Received 2011 December 9; in original form 2011 September 21

ABSTRACT

We examine the impact of helium reionization on the structure of the intergalactic medium. We model the reionization using a radiative transfer (RT) code coupled to the combined gravity hydrodynamics code ENZO. Neutral hydrogen and helium are initially ionized by a starburst spectrum, which is allowed to gradually evolve into a power-law spectrum over the redshift interval $3.0 < z < 4.0$. The temperature–density relation of the gas is found to fan out and flatten following He II reionization, with an inversion for high overdensities of $\rho/\langle\rho\rangle > 5$. Peculiar velocities of up to $10\,\mathrm{km\,s^{-1}}$ are induced by the increased pressure, with the gas density field distorted over large coherent regions by 10–20 per cent, and the dark matter by levels of 1 per cent. The photoionization-induced flows may thus distort the matter power spectrum at comoving wavenumbers $k > 0.5\,h\,\mathrm{Mpc^{-1}}$ by a few per cent by $z = 2$.

Absorption spectra for H I and He II are drawn from the simulations, and absorption lines are fitted to the spectra. The increased temperature following He II reionization reduces the line centre optical depths, resulting in an enhancement in the fraction of very low optical depth pixels and an overall distortion in the pixel flux distribution compared with He II reionization in the optically thin limit. A median Doppler parameter of $35\,\mathrm{km\,s^{-1}}$ is obtained for the H I absorption systems at $z = 3$. Dividing into subsamples optically thick and optically thin at line centre reveals that the optically thick systems undergo only mild evolution while the optically thin systems evolve rapidly following He II reionization. A comparison between He II and H I absorption features shows a broad distribution in the He II and H I column density ratio, although much of the width is an artefact of the deblending of the absorption features by the line fitting. The distribution of the ratio of He II and H I Doppler parameters peaks midway between the thermally broadened and velocity-broadened limits. A comparison with approximate simulation methods based on either a pseudo-hydrodynamical scheme or a non-RT hydrodynamical simulation with boosted He II heating rate shows moderately good agreement in the absorption line properties, but not to the precision to which they may be measured, and not over the full redshift range for which the high-redshift Lyα forest is observed.

Key words: radiative transfer – quasars: absorption lines – quasars: general – large-scale structure of Universe.

1 INTRODUCTION

Cosmological simulations of the intergalactic medium (IGM) in the context of cold dark matter(CDM) theories for structure formation have proven extremely successful in reproducing many of the observed properties of the IGM as measured through the Lyα forest. The mean H I transmission through the IGM is recovered for an H I ionizing background matching that of the measured quasi-stellar object (QSO) luminosity function for $z < 3$, although an enhanced radiation field, likely due to galaxies, is required at higher redshifts. Once normalized to the mean transmission, the H I column density distribution is broadly recovered as well for a ΛCDM model, as is the measured power spectrum of the H I flux. See Meiksin (2009) for a review.

Despite these successes, some of the statistics still show lack of agreement with measured values. Prominent among these is

★E-mail: A.Meiksin@ed.ac.uk
†Scottish Universities Physics Alliance.

the line widths of the H I absorption features, which tend to be broader than the predictions (Bryan & Machacek 2000; Theuns, Schaye & Haehnelt 2000). A detailed comparison with measured spectra reveals that the disagreement is among the optically thin Lyα systems, for which an additional contribution of 10–15 km s^{-1}, added in quadrature to the Doppler parameter, is required, while the widths of the optically thick systems well match the measured values (Meiksin, Bryan & Machacek 2001). One possible explanation is recent heat input at $z \lesssim 4$ into the IGM. The additional required broadening corresponds to a temperature increase of 17×10^3 K. The optically thin systems are associated with moderate density or even underdense structures for which the time to reach thermal equilibrium exceeds a Hubble time (Meiksin 1994; Miralda-Escudé & Rees 1994). The optically thin systems may thus retain a memory of recent heat input at $z \lesssim 4$.

The most likely source of heating is He II reionization. The abundance of QSOs suggests they would have ionized He II at a redshift $3 < z_{\rm He\,II} < 4.5$, although possibly as early as $z_{\rm He\,II} \simeq 5$ for sufficiently hard spectra (Meiksin 2005). Support for recent He II reionization has been based on measurements of the He II Lyα optical depth of the IGM. The measurements span the redshift range $2.2 < z < 3.8$ based on *Hubble Space Telescope* (*HST*) observations of Q0302−003 ($z_{\rm em} \simeq 3.3$) (Jakobsen et al. 1994; Heap et al. 2000), *Hopkins Ultraviolet Telescope* and *Far Ultraviolet Spectroscopic Explorer* (*FUSE*) observations of HS 1700+6416 ($z_{\rm em} \simeq 2.7$) (Davidsen, Kriss & Zheng 1996; Fechner et al. 2006), *HST* and *FUSE* observations of HE 2347−4342 ($z_{\rm em} \simeq 2.9$) (Reimers et al. 1997; Kriss et al. 2001; Smette et al. 2002; Shull et al. 2010), and *HST* observations of PKS 1935−692 ($z_{\rm em} \simeq 3.2$) (Anderson et al. 1999), SDSS J2346−0016 ($z_{\rm em} \simeq 3.5$) (Zheng et al. 2004a, 2008), Q1157+3143 ($z_{\rm em} \simeq 3.0$) (Reimers et al. 2005), SDSS J1711+6052 ($z_{\rm em} \simeq 3.8$) (Zheng et al. 2008), and SDSS J1101+1053 ($z_{\rm em} \simeq 3.0$) and SDSS J0924+4852 ($z_{\rm em} \simeq 3.0$) (Worseck et al. 2011). The He II Lyα optical depths rise rapidly from $\tau_{\rm He\,II} \simeq 1.00 \pm 0.07$ averaged over the redshift interval $z = 2.2$–2.6 to $\tau_{\rm He\,II} \simeq 4.9$ at $z \simeq 3.3$ (Syphers et al. 2011a), as if entering into the epoch of He II reionization.

The origin of the UV background, however, is still not well established. The high He II Lyα optical depths compared with the corresponding values found for H I generally requires that the UV metagalactic background be soft between the He II and H I photoelectric edges, with a ratio of H I to He II photoionization rates of $\Psi > 200$ at $z \approx 3$ (Madau & Meiksin 1994), corresponding to a source spectral index for $f_\nu \sim \nu^{-\alpha_{\rm S}}$ of $\alpha_{\rm S} > 1.8$ after allowing for the filtering of the radiation through the IGM (Madau & Meiksin 1994; Haardt & Madau 1996; Bolton et al. 2006). This is consistent with the inferred spectral index of bright high-redshift ($0.3 < z < 2.3$) QSOs after correcting for IGM absorption (Telfer et al. 2002), but it is inconsistent with the much harder spectra found for dimmer QSOs nearby ($z < 0.67$) (Scott et al. 2004), for which minimal IGM corrections are required. Possibly ionizing radiation from galaxies boosts the H I photoionization rate, however the contribution from QSOs alone approximately matches the required rate to recover the measured H I Lyα optical depth (Bolton et al. 2005; Meiksin 2005), leaving little room for additional sources.

The optical depth measurements are moreover found to fluctuate over a wide range at a given redshift. This is most dramatically illustrated by measurements of the He II Lyα forest compared with the corresponding measurements of H I. A wide spread is found for the column density ratio $\eta = N_{\rm He\,II}/N_{\rm H\,I}$, varying at least over the range $4 < \eta < 600$ at $2.3 < z < 2.8$ (Zheng et al. 2004b; Reimers et al. 2005; Fechner et al. 2006; Shull et al. 2010). The higher values correspond to H I to He II photoionization rate ratios of $\Psi > 1000$. Such fluctuations are expected during the epoch of He II reionization, so that the large He II Lyα optical depth values may result from a mean over regions in which most of the helium is still in the form of He II.

The interpretation is not unique, however. Due to the discreteness of the sources of ionizing radiation and attenuation by the IGM, local fluctuations are expected in the UV metagalactic background (Zuo 1992; Fardal, Giroux & Shull 1998; Meiksin & White 2003). The distribution of fluctuations in η measured in HE 2347−4342 is well matched by a UV background dominated by QSOs with a soft spectral index consistent with the data of Telfer et al. (2002) (Shull et al. 2004; Fardal et al. 1998; Bolton et al. 2006), as is the distribution of η fluctuations measured in HS 1700+6416 (Meiksin 2009). Alternatively, harder QSO spectra could be accommodated if additional H I ionizing sources other than QSOs were present, but, again, there is not much room to add more sources without over-ionizing the hydrogen. The full range of fluctuations in the measured values of $\tau_{\rm He\,II}$ in several QSO lines of sight suggests the epoch of He II reionization may have completed as recently as $z \simeq 2.9$ (Furlanetto & Dixon 2010; Shull et al. 2010; Worseck et al. 2011). By contrast, recent attempts to quantify the thermal evolution of the IGM from the H I Lyα forest measured in QSO spectra indicate a rise in the temperature of gas at the mean density for $z \simeq 4$ (Becker et al. 2011), suggesting He II reionization was becoming widespread at these times. If both interpretations are correct, then He II reionization was a drawn out process extending over the redshift range $2.9 \lesssim z \lesssim 4.5$.

The primary purpose of this paper is to investigate the dynamical impact of helium reionization on the structure of the IGM and its observational signatures. While early simulations of the IGM included helium reionization, they were done in the optically thin limit. Cosmological simulations solving the radiative transfer (RT) equation during helium reionization were restricted to the gravitational component, which was used to scale the baryonic component properties (Tittley & Meiksin 2007; McQuinn et al. 2009). In this paper, we implement RT using the algorithms of Abel, Norman & Madau (1999) and Bolton, Meiksin & White (2004) coupled to the gravity-hydrodynamics code ENZO[1] (specifically v.1.0.1). The hydrodynamical response of the gas to the boost in heating when RT is included could result in more rapid photoevaporation of the gas in small haloes, allowing reionization to occur more rapidly, as well as in observational signatures on the Lyα forest such as increased line broadening due to outflows from the haloes and a decrease in the ratio of gas density to dark matter density. An increase in the gas temperature will also alter the ionization fractions of hydrogen and helium at a given gas density, producing modifications to the column densities of the absorption features, the distribution function of pixel fluxes, and the flux power spectrum, all basic statistics used to quantify the Lyα forest and the predictions of cosmological models for its structure.

A secondary purpose is to assess the degree to which approximate treatments of the reionization reproduce the results from a fully coupled radiative hydrodynamics scheme. An approximate treatment that produced results that agree well with the full computation would offer substantial computational savings, permitting a wider range of reionization models to be explored. Accordingly, a parallel suite is performed of reionization simulations using ENZO in the optically thin approximation, including a set with a boosted He II heating

[1] Available from http://lca.ucsd.edu.

rate, as well as a set using our previous pseudo-hydrodynamical simulations with RT.

All results are for a flat ΛCDM universe with the cosmological parameters $\Omega_{\rm m} = 0.24$, $\Omega_{\rm b}h^2 = 0.022$ and $h = H_0/100\,{\rm km\,s^{-1}} = 0.73$, representing the total mass density, baryon density and Hubble constant, respectively. The power spectrum has spectral index $n = 0.95$, and is normalized to $\sigma_{8h^{-1}} = 0.74$, consistent with measurements by the *Wilkinson Microwave Anisotropy Probe* (Larson et al. 2011).

This paper is organized as follows. Estimates for the expected IGM temperature boost following He II reionization are discussed in the next section. The simulations are described in Section 3 and the results presented in Section 4. The H I and He II spectral signatures of He II reionization are presented in Section 5. A comparison with approximate simulation methods is provided in Section 6. The principal conclusions are summarized in the final section.

2 PHOTOIONIZATION HEATING

A radiation field with its specific energy density locally approximated near the He II photoelectric edge by $u_\nu = u_{\rm L}(\nu/\nu_{\rm L})^{-\alpha}$ will photoionize the He II at the rate per He II ion:

$$\Gamma_{\rm He\,II} = \int {\rm d}\nu\, \frac{cu_\nu}{h_{\rm P}\nu}\sigma_\nu \simeq h_{\rm P}^{-1}c\sigma_0\frac{u_{\rm L}}{3+\alpha}, \quad (1)$$

where $\nu_{\rm L}$ is the frequency of the He II Lyman edge, the photoionization cross-section is approximated as $\sigma \simeq \sigma_0(\nu/\nu_{\rm L})^{-3}$ and $h_{\rm P}$ is the Planck constant. The corresponding heating rate per He II ion is

$$\begin{aligned} G_{\rm He\,II} &= \int {\rm d}\nu\, \frac{cu_\nu}{h_{\rm P}\nu}(h_{\rm P}\nu - h_{\rm P}\nu_{\rm L})\sigma_\nu \\ &\simeq c\sigma_0\nu_{\rm L}\frac{u_{\rm L}}{(2+\alpha)(3+\alpha)}. \end{aligned} \quad (2)$$

The heating rate per ionization, normalized by the ionization potential, is then $\epsilon_{\rm He\,II} = G_{\rm He\,II}/(h_{\rm P}\nu_{\rm L}\Gamma_{\rm He\,II}) = 1/(2+\alpha)$. The energy injected into the gas is thus sensitive to the shape of the local ionizing spectrum. A hardened radiation field with $\alpha < 0$ can result in a large amount of energy deposited per ionization.

The spectrum is expected to harden within an ionization front because hard photons are less likely to be absorbed than soft photons above the photoelectric threshold for a given optical depth at the threshold energy. In general, for a column density N the optical depth above the photoelectric threshold of hydrogen or singly ionized helium is $\tau_\nu \simeq \tau_{\rm L}(\nu/\nu_{\rm L})^{-3}$, where $\tau_{\rm L} = \sigma_0 N$. The photoionization rate per atom/ion may be expressed in terms of the incident radiation density from the source $u_\nu^{\rm S} = u_{\rm L}^{\rm S}(\nu/\nu_{\rm L})^{-\alpha_{\rm S}}$ as

$$\begin{aligned} \Gamma &= \int_{\nu_{\rm L}}^{\infty} {\rm d}\nu\, \exp\left[-\tau_{\rm L}\left(\frac{\nu}{\nu_{\rm L}}\right)^{-3}\right]\frac{cu_{\rm L}^{\rm S}\sigma_0}{h_{\rm P}\nu}\left(\frac{\nu}{\nu_{\rm L}}\right)^{-(3+\alpha_{\rm S})} \\ &= \frac{1}{3}\frac{cu_{\rm L}^{\rm S}}{h_{\rm P}N}\tau_{\rm L}^{-(1/3)\alpha_{\rm S}}\gamma\left(1+\frac{1}{3}\alpha_{\rm S},\tau_{\rm L}\right), \end{aligned} \quad (3)$$

where $\gamma(a,x) = \int_0^x {\rm d}t\, {\rm e}^{-t}t^{a-1}$ is the incomplete gamma function. Similarly, the heating rate per atom/ion is

$$\begin{aligned} G &= \int_{\nu_{\rm L}}^{\infty} {\rm d}\nu\, \exp\left[-\tau_{\rm L}\left(\frac{\nu}{\nu_{\rm L}}\right)^{-3}\right]\frac{cu_{\rm L}^{\rm S}\sigma_0}{h_{\rm P}\nu}\left(\frac{\nu}{\nu_{\rm L}}\right)^{-(3+\alpha_{\rm S})} \\ &\quad\times(h_{\rm P}\nu - h_{\rm P}\nu_{\rm L}) \\ &= \frac{1}{3}\frac{cu_{\rm L}^{\rm S}\nu_{\rm L}}{N}\tau_{\rm L}^{-(1/3)\alpha_{\rm S}} \\ &\quad\times\left[\tau_{\rm L}^{1/3}\gamma\left(1+\frac{\alpha_{\rm S}-1}{3},\tau_{\rm L}\right) - \gamma\left(1+\frac{1}{3}\alpha_{\rm S},\tau_{\rm L}\right)\right]. \end{aligned} \quad (4)$$

The resulting heating rate per ionization of He II will produce a temperature increment:

$$\Delta T = \frac{2}{3}\frac{h_{\rm P}\nu_{\rm L}}{k_{\rm B}}\frac{\epsilon_{\rm He\,II}}{2\frac{n_{\rm H}}{n_{\rm He}}+3} - \frac{T_{\rm i}}{2\frac{n_{\rm H}}{n_{\rm He}}+3}, \quad (5)$$

where $T_{\rm i}$ is the initial gas temperature and $k_{\rm B}$ is the Boltzmann constant. The increment corresponds to the complete ionization of He II to He III at fixed $\tau_{\rm L}$, as would occur in the presence of an intervening Lyman limit system, already in ionization equilibrium, lying between the source and the region being photoionized if the Lyman limit system dominated the optical depth at the Lyman edge. The radiation field reaching the region being photoionized would be hardened by the absorption within the intervening system. The temperature increment is shown as a function of the optical depth $\tau_{\rm L}$ at the He II Lyman edge for a range of source spectral indices in Fig. 1 (upper set of curves). A helium mass fraction of $Y = 0.248$ was adopted (Steigman 2007). A system with overdensity $\rho/\langle\rho\rangle$ and comoving thickness L would have an optical depth at the He II Lyman edge of

$$\tau_{\rm L,He\,II} \simeq 115\frac{\rho/\langle\rho\rangle}{100}\frac{(1+z)^2}{16}\frac{L}{1\,{\rm Mpc}}. \quad (6)$$

The radiation hardening through overdense systems with $\rho/\langle\rho\rangle \sim 200$ and comoving sizes of 0.05–0.25 kpc would produce temperature boosts in the 'shadows' they cast in less dense, more quickly photoionized structures, of up to $\Delta T \simeq 40\,000$ K, and even reaching 10^5 K in the shadows of intervening systems with $\tau_{\rm L,He\,II} > 100$.

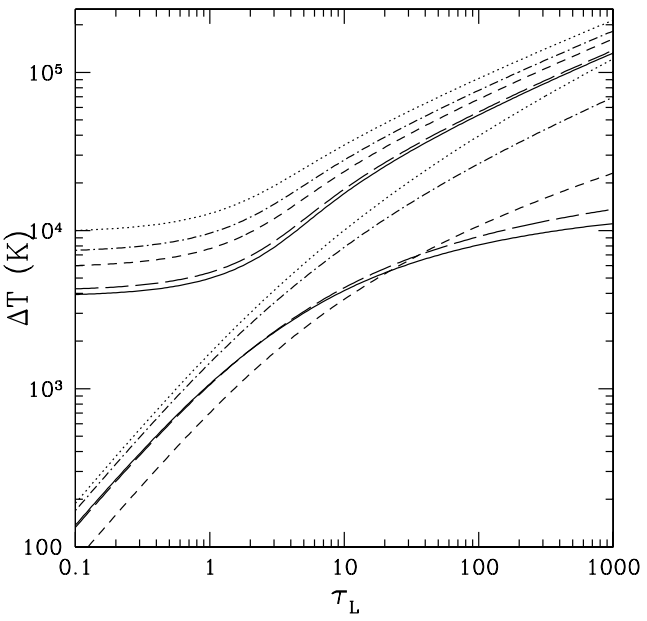

Figure 1. Temperature increment for ionizing He II to He III as a function of the optical depth $\tau_{\rm L}$ at the He II Lyman edge, prior to the onset of radiative recombinations. Shown for a source spectrum $f_\nu \propto \nu^{-\alpha_{\rm S}}$ with spectral index $\alpha_{\rm S} = 1.8$ (solid line), 1.5 (long-dashed line), 0.5 (short-dashed line), 0 (dot–dashed line) and −0.5 (dotted line). The upper set of curves corresponds to reionization going to completion at a fixed optical depth, as would occur for radiation filtered through a foreground absorption system in ionization equilibrium. The temperature boost increases for harder source spectra. For large $\tau_{\rm L}$, the temperature boost increases like $\tau_{\rm L}^{1/3}$. The lower set of curves corresponds to the temperature boost for a time varying optical depth as an ionization front sweeps through a slab of material with an initial optical depth $\tau_{\rm L}(0)$ given by the value $\tau_{\rm L}$ indicated. Very high temperatures are reached for hard spectra.

Radiative recombination and excitation atomic line cooling will subsequently lower the temperature of the gas once the ionization front has passed, although the equilibrium temperature may never be achieved in rarefied underdense regions because of the long required time-scales (Meiksin 1994; Miralda-Escudé & Rees 1994).

Alternatively, the heating produced by the passage of an ionization front through a slab of gas in which the optical depth decreases as the ionization front sweeps through may be approximated, before recombinations become important, by equating the incident rate of ionizing photons with the rate at which the gas in the slab is photoionized. For an initial optical depth $\tau_{\rm L}(0)$ at the Lyman edge, the Lyman edge optical depth will evolve according to

$$\tau_{\rm L}(t) = \tau_{\rm L}(0)\left[1 - k\frac{cu_{\rm L}^{\rm S}}{h_{\rm P}}\frac{\sigma_0}{\tau_{\rm L}(0)}t\right], \quad (7)$$

where $k = 1/\alpha_{\rm S}$ for $\alpha_{\rm S} > 0$, $k = \log(\nu_{\rm max}/\nu_{\rm L})$ for $\alpha_{\rm S} = 0$ and $k = [(\nu_{\rm max}/\nu_{\rm L})^{-\alpha_{\rm S}} - 1]/(-\alpha_{\rm S})$ for $\alpha_{\rm S} < 0$, where $\nu_{\rm max}$ is the maximum frequency for which photoionizing photons are produced. Using equations (3) and (4) for the photoionization and heating rates, the number density n of the species undergoing ionization and the thermal energy input per unit volume u, as a function of $\tau_{\rm L}$, are governed by

$$\frac{{\rm d}\log n}{{\rm d}\tau_{\rm L}} = \frac{1}{3k\tau_{\rm L}^{1+\alpha_{\rm S}/3}}\gamma\left(1+\frac{\alpha_{\rm S}}{3},\tau_{\rm L}\right) \quad (8)$$

and

$$\frac{{\rm d}u}{{\rm d}\tau_{\rm L}} = -\frac{1}{3}\frac{nh\nu_{\rm L}}{k\tau_{\rm L}^{1+\alpha_{\rm S}/3}}\left[\tau_{\rm L}^{1/3}\gamma\left(1+\frac{\alpha_{\rm S}-1}{3},\tau_{\rm L}\right) - \gamma\left(1+\frac{\alpha_{\rm S}}{3},\tau_{\rm L}\right)\right]. \quad (9)$$

The resulting post-ionization temperature is shown in Fig. 1 (lower set of curves). Temperature boosts of ∼1000–10 000 K are typical, although hard spectra sources ($\alpha_{\rm S} < 0$) can produce substantially higher temperatures. (Somewhat arbitrarily, $\nu_{\rm max}/\nu_{\rm L} = 4$ was assumed for $\alpha_{\rm S} \leq 0$.) Again, radiative recombination and excitation line cooling will eventually decrease the gas temperature.

Temperature boosts following He II reionization typically ranging between $\Delta T \simeq 5000$ and 20 000 K at $z = 3$, but reaching as high as $\Delta T \simeq 30\,000$–40 000 K directly after reionization, were found in the reionization simulations of Tittley & Meiksin (2007) for a source with spectral index $\alpha_{\rm S} = 0.5$, turning on after a starburst-like spectrum photoionizes the hydrogen and neutral helium to singly ionized helium. For a pure power-law source spectrum ($\alpha_{\rm S} = 0.5$) and for a mini-quasar spectrum, lower overall temperatures of 5000–20 000 K were obtained at $3 < z < 4$. Higher temperatures were generally found in the denser structures. Temperature boosts of $\Delta T \simeq 10\,000$–20 000 K were found by McQuinn et al. (2009) for a QSO spectral distribution with a mean spectral index of $\alpha_{\rm S} = 1.2$, and boosts of up to $\Delta T \simeq 30\,000$ K were found for harder source spectra with a mean spectral index $\alpha_{\rm S} = 0.6$.

In addition to cooling by atomic processes, the gas will undergo adiabatic cooling losses as it escapes from gravitational potential wells that were able to bind the gas when cooler. The expansion velocities will also broaden the absorption features (Meiksin 1994). Previous He II reionization simulations, which used the dark matter distribution to model the baryon density, were not able to take these effects into account. In this paper, we take the hydrodynamical response of the gas into account by coupling our RT scheme to a gravity-hydrodynamics code.

3 SIMULATIONS

We have modified the combined hydrodynamics N-body gravity code ENZO by replacing its ionization and atomic cooling modules by ones employing the methods used by Tittley & Meiksin (2007). In summary, the probabilistic RT method of Abel et al. (1999), extended to include helium by Bolton et al. (2004), is used to compute the reionization of both hydrogen and helium. Atomic cooling from the radiative recombination of the hydrogen and the two helium states is included, along with collisional excitation of neutral hydrogen and Compton cooling. Cooling due to the collisional ionization of hydrogen and the collisional excitation and ionization of helium are negligible for the temperatures encountered in the simulations.

For the hydrodynamical processes at the resolution of cosmological IGM simulations, the dynamical time-scales are much longer than the radiative time-scales in the vicinity of the ionization front. It would be prohibitively expensive computationally and unnecessary to force the hydrodynamics to evolve at the same time-scale as the RT. Hence, in our implementation the RT time-scale is allowed to drop below that of the hydrodynamics.

The energy equation is solved through operator splitting by computing the ionization state of the gas and the amount of photoionization heating and atomic cooling between the hydrodynamical time steps. During the ionization time steps, all parameters of the gas are taken to be those at the end of the immediately preceding hydrodynamical time step with the exception of the fluid density and temperature. The density is varied linearly from the previous hydrodynamical time step to that of the current ionization time step while the RT processes along with the gas temperature are evolved on their own, shorter, adaptive time-scale. Heating and cooling within the RT step modify only the gas entropy leaving adiabatic compressional heating to ENZO's hydrodynamic functions.

The probabilistic RT method fails for discrete intervals with large optical depths, τ. To overcome this, the RT code refines any discrete path length in which $\tau > 1$ and for which the cumulative optical depth between the source and the interval is small: $\tau_{\rm Cumulative} < 2$. These two conditions select optically thick intervals seeing a weakly attenuated ionizing source, i.e. the ionizing front. Refinement consists of dividing the interval into a series of shorter intervals and recursively performing RT.

The RT code is modified from that used in Tittley & Meiksin (2007) by now adopting case B recombination and heating coefficients within refinements. Case B coefficients assume any recombinations to the ground state lead to the emission of a photon which immediately ionizes a local atom, so that only recombinations to excited states contribute to local ionization balance.

Several studies on the convergence of the absorption line features have emphasized the need for both large boxes and high spatial resolution (Theuns et al. 1998; Bryan et al. 1999; Meiksin & White 2001, 2004; Bolton et al. 2005). Achieving convergence on the flux and line parameter distributions to 10 per cent accuracy at $z > 2$ requires resolving the Jeans length and a simulation volume of at least $25\,h^{-1}$ Mpc on a side (Meiksin & White 2004; Bolton et al. 2005). Convergence to much higher precision is considerably more demanding, requiring resolution of the Jeans length as well as box sizes of at least 40–$80\,h^{-1}$ Mpc, depending on redshift (Bolton & Becker 2009; Tytler et al. 2009).

The ENZO simulations were carried out in a box $25\,h^{-1}$ Mpc (comoving) on a side. This corresponds to the order of the expected size of a He II ionization front at the helium reionization epoch, when the characteristic size of the He III zone produced collectively by

multiple QSO sources is comparable to the mean distance between QSOs, which is typically ∼50 Mpc (comoving) at $z \simeq 3$ (Wolf et al. 2003; Meiksin 2005). The simulations were performed with 512^3 gravitating particles and 256^3 grid zones for the fluid component, corresponding to a resolution of 98 kpc (comoving), sufficient to resolve the Jeans length.

An effect neglected in the simulations is the role played by the subsequent overlap of other incoming He II ionization fronts. For gas in which helium has already been photoionized, these will have little effect on the temperature and dynamics of the gas, since the temperature of gas once photoionized is largely insensitive to the intensity of the radiation field that maintains the photoionization. Pockets of gas that have not yet been photoionized to He III, however, will respond to incoming fronts, with a consequent boost in temperature and expansion. These effects should only become important towards the end of the helium reionization epoch. They should, of course, be included in a complete simulation of intergalactic helium reionization.

Because of its high computational expense, RT was performed within a limited slice through the simulation volume. In the PMRT run where gas density is inferred from a PM code, there is no advection of gas properties so a single slice was sufficient. For the ENZO runs, which allow for advection of gas properties, RT was performed on five slices, with only the central slice used in the analysis. The surrounding sets of two slices provide a buffer between the slice and the volume that is unirradiated. The choice of padding depth was chosen by a suite of convergence tests to a tolerance of 1 per cent. Excepting that the slice used in the analysis was selected to match in each of the simulations, the selection was otherwise arbitrary.

The incident spectrum, shown in Fig. 2, corresponds to a hybrid starburst–QSO model as in Tittley & Meiksin (2007): an initial starburst spectrum is turned on at $z = 8$ and transformed into a power-law spectrum $f_\nu \propto \nu^{-0.5}$. The power-law spectrum is initially turned on at $z = 4$, then ramped up to its full value by $z = 3$ while the starburst spectrum is ramped down during the same interval. The incident flux at the edge of the box is

$$\mathcal{F}_\nu = \frac{L_\nu}{4\pi\,(aR_0)^2}, \tag{10}$$

where the luminosity at the Lyman edge $L_{\nu_{\rm L}} = 10^{23} J\,{\rm s}^{-1}{\rm Hz}^{-1}$ for the starburst spectrum and $L_{\nu_{\rm L}} = 2.62 \times 10^{21}\,J\,{\rm s}^{-1}\,{\rm Hz}^{-1}$ for the power law. The QSO-like power-law spectrum is normalized to produce half the number of hydrogen-ionizing photons as the starburst. A comoving distance of $aR_0 = a5\,{\rm Mpc}\ h^{-1}$ dilutes the unattenuated flux which is held uniform through the slice.

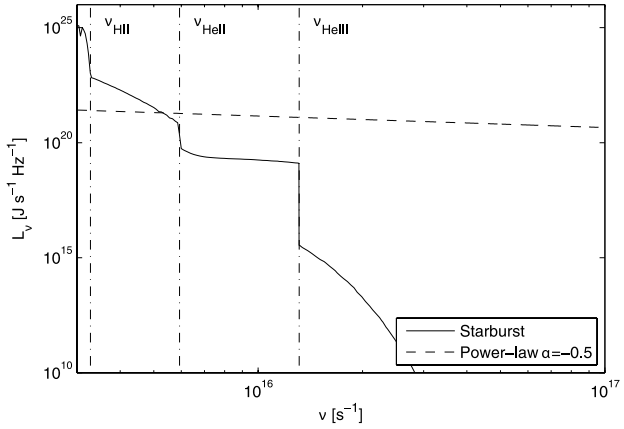

Figure 2. The incident spectrum begins as a starburst spectrum at $z = 8$ which linearly transforms to an $\alpha = -0.5$ power-law spectrum between $z = 4$ and 3 henceforth being simply a power law.

Table 1. Identifiers for the various simulations used in this paper.

	ENZO[a]	PM[b]	RT[c]	OT[d]	$2G_{\rm He\,II}$[e]
ENZO	•				
EnzoRT	•		•		
EnzoOT	•			•	
EnzoOT+$2G_{\rm He\,II}$	•			•	•
PMRT		•	•		

[a] Gas evolved by full hydrodynamical code ENZO.
[b] Gas evolved by N-body particle mesh code.
[c] Radiative ionization and heating calculated using RT equations.
[d] Radiative ionization and heating calculated using optically thin approximation for hydrogen and helium.
[e] Heating from He II ionization boosted by a factor of 2.

Integration over the spectrum to determine the ionization and ionization heating rates is made difficult by the sharp discontinuities at the ionization edges, inherent in the starburst spectrum and induced in the power-law spectrum by attenuation. The discontinuities are avoided by breaking the integration into three intervals: $\nu_{\rm H\,II}$ to $\nu_{\rm He\,II}$, $\nu_{\rm He\,II}$ to $\nu_{\rm He\,III}$ and $\nu_{\rm He\,III}$ to ∞. We use Gauss–Legendre quadrature for the first two intervals and Gauss–Laguerre for the final with 16, 8 and 32 samples respectively, based on convergence tests.

While the bulk of what we present in this paper is the result of a cosmological simulation with the gas subjected to an ionizing radiation field solved with RT, a number of simulations were run primarily to test the utility of less numerically intensive methods. These other simulations also provide insight into the significance of radiative and hydrodynamic processes. The simulations had the identical initial conditions or, in the case of the simulation with the gas density inferred from a PM code, the identical initial dark matter distribution. The notation for the different simulations is summarized in Table 1.

4 RESULTS

4.1 Physical impact

The intensity of the starburst spectrum was adjusted to ensure the hydrogen ionization front swept across the simulation volume by $z \simeq 6$, although some shadowed regions persist along the edge of the box until $z \simeq 5.5$. The intensity of the power-law spectrum was adjusted so that the He II ionization front swept across the box by $z \simeq 3.2$, again with some shadowing persisting to $z \lesssim 3$.

The heating rate per ionization of He II as the He II ionization front passes through the box at $z = 3.3$ is shown in Fig. 3. The filtering effect of the IGM in hardening the ionizing radiation field is clearly discernible in the pre-ionized gas ahead of the ionization front. The heating rate per ionization is substantially enhanced, reaching values of up to 100–400 eV. By comparison, once the front has passed, the energy per He II ionization is ∼22 eV.

The resulting temperature structure is shown in Fig. 4 as the He II ionization front passes through the box at $z = 3.3$ and at $z = 2.0$, after He II ionization has completed. The effects of shadowing produced by density inhomogeneities in the IGM are apparent as the advance of the ionization front is delayed beyond the densest

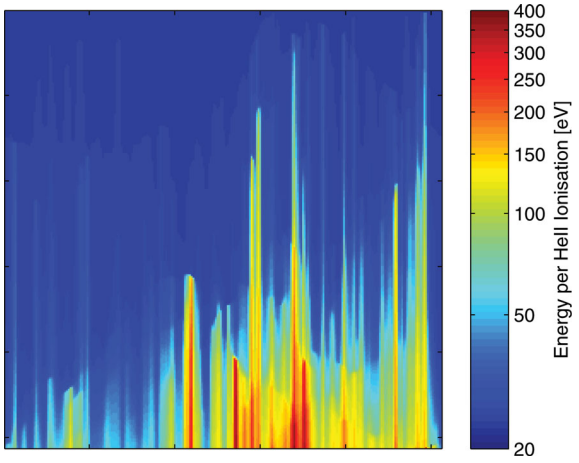

Figure 3. The heating rate per He II ionization at $z = 3.3$ for a He II ionization front sweeping across the box from top to bottom in the EnzoRT run. The box is $25\,h^{-1}$ Mpc on each side, from which a slice $25\,000/256 \simeq 100\,h^{-1}$ kpc thick is extracted.

regions. This may best be seen by comparing the temperature map at $z = 3.3$ in Fig. 4 with the density map in Fig. 5. (The principal density structures change little between $z = 3.3$ and 2.0 in comoving coordinates.) Large temperature boosts of 3–4 $\times$ 10^4 K occur downstream from dense clumps, consistent with the striations of high heating rates per ionization in Fig. 3 as expected for photoionization by a radiation field hardened by intervening optically thick clumps with optical depths of several tens, as discussed in Section 2.

By $z = 2.0$, most of the high-temperature striations have been replaced by gas temperatures that trace the matter distribution now that He II reionization has completed. Pronounced hot regions, however, persist, particularly in underdense regions unable to achieve thermal equilibrium. These lay behind dense structures while the gas was re-ionized. The filtering of the radiation field by the dense structures hardened the spectrum of the incident radiation passing downstream to the underdense gas, as shown in Fig. 3, producing the high temperatures. This effect is especially prevalent in the centre-right portion of the figure.

4.2 Differential impact

Including RT in the ionization of He II substantially boosts the temperature of the gas, increasing it typically by 15–20 $\times$ 10^3 K over the optically thin reionization limit, as shown in Fig. 6. The temperature–density relation is shown in Fig. 7. The plateau with a gas temperature of $\sim$20–30 $\times$ 10^3 K at the mean baryon density agrees well with the estimate of Schaye et al. (2000) of $T_0 \sim 20$–30 $\times$ 10^3 K at $z = 3$, with only a weakly increasing temperature with overdensity, as inferred from the Doppler widths measured in high-resolution spectra of the Lyα forest. The temperature found in the simulation, however, is much larger than the temperature at the mean density of $T_0 \sim 10$–15 $\times$ 10^3 determined from the flux curvature method applied to high-resolution data (Becker et al. 2011). The discrepancy may be due to an inadequate simulation model for calibrating the statistic used to estimate the gas temperature. Alternatively, it may indicate that either He II was re-ionized too late in the simulation here, or that the He II ionizing source was too hard. A temperature inversion occurs for $\rho/\langle\rho\rangle > 5$, as is expected for thermal balance between photoionization heating and atomic line and radiative recombination cooling in dense structures. Only such high-density gas is able to achieve thermal balance; the time-scale to achieve equilibrium is too long in underdense gas (Meiksin 1994; Miralda-Escudé & Rees 1994). A similar trend between temperature and density is found for a pure dark matter simulation with RT (Tittley & Meiksin 2007).

Compared with optically thin reionization, the excess temperature boost allowing for RT occurs primarily for underdense gas, as shown in Fig. 7 (right-hand panel). Most of the gas with $\rho/\langle\rho\rangle > 3$ experiences very little boost at all, as it is able to quickly recover thermal balance.

A map of the difference in the temperatures is shown in Fig. 8. Boosts of $\Delta T > 15 \times 10^3$ K are visible downstream of very dense structures which act to filter and harden the radiation field passing through them. The densest structures themselves show little change in temperature, as the temperature rapidly reaches thermal balance. Small overdense patches, however, show marked temperature deficits, as much as $\Delta T < -10 \times 10^3$ K. These regions account for the temperature reductions in the right-hand panel of Fig. 7. The temperature decreases arise from complete shadowing of the He II

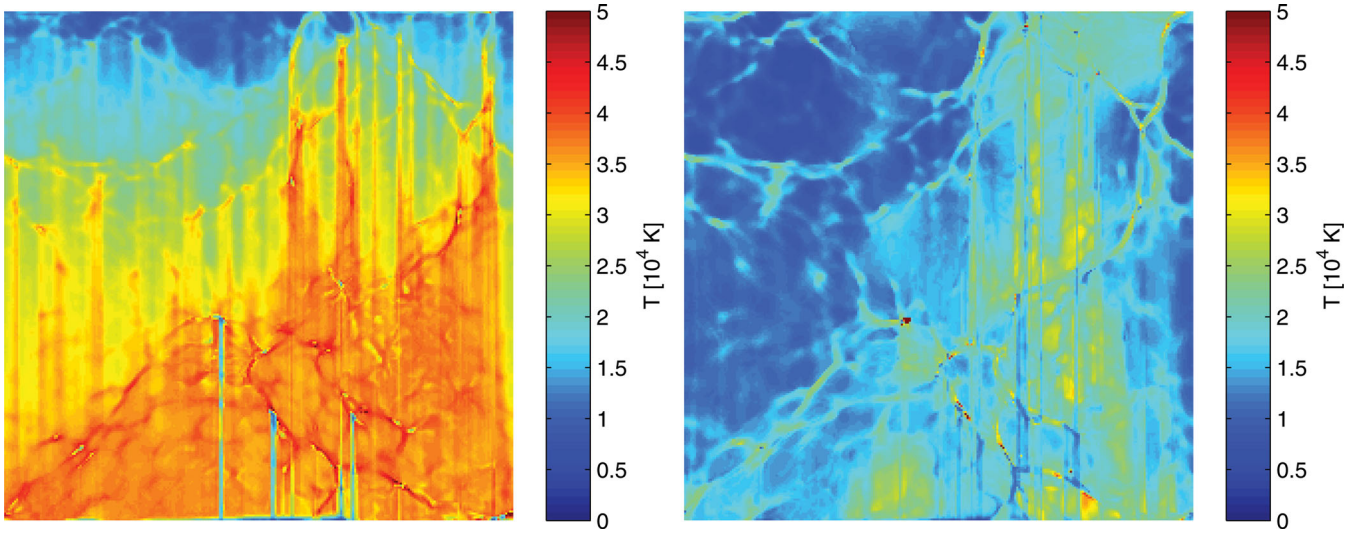

Figure 4. The post-ionization temperature for a He II ionization front sweeping across a slice in the box from top to bottom, at $z = 3.3$ (left-hand panel) and $z = 2.0$ (right-hand panel). The box side is $25h^{-1}$ Mpc (comoving).

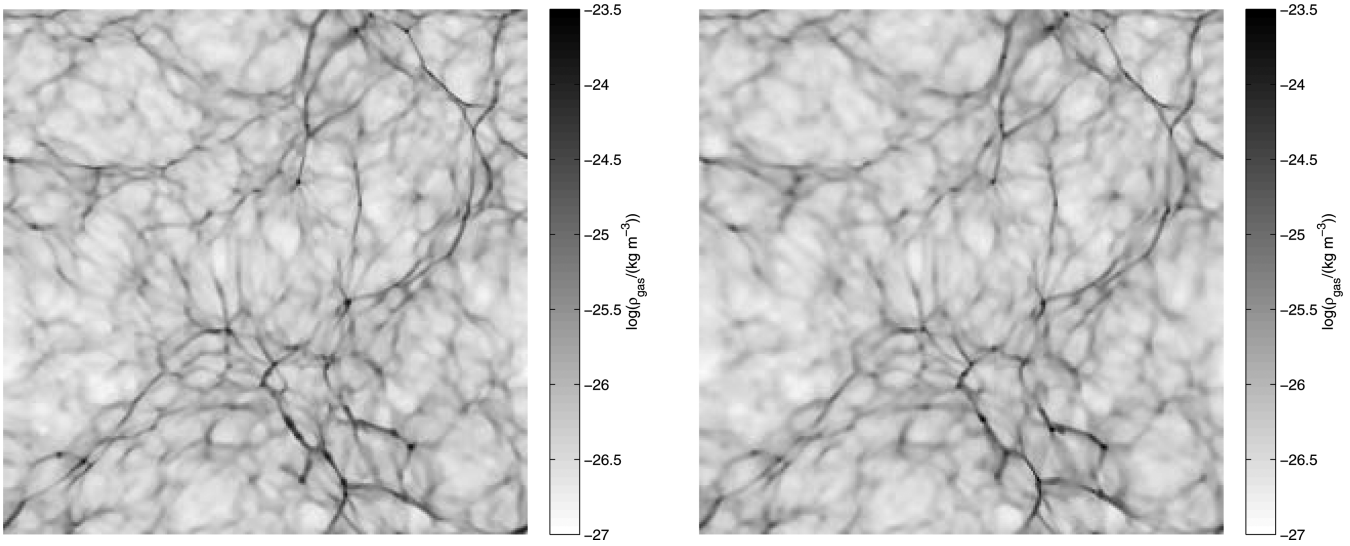

Figure 5. The gas distribution at $z = 2.0$ without He II reionization (left-hand panel) and with (right-hand panel), corresponding to Fig. 4. Gas is driven out of small haloes by the He II reionization. The box side is $25\,h^{-1}$ Mpc (comoving).

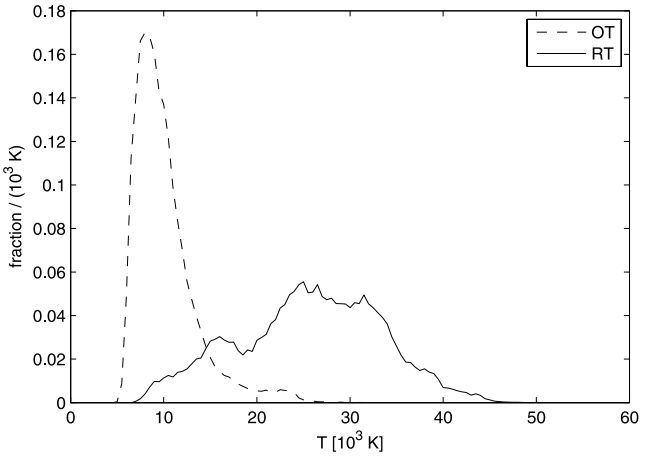

Figure 6. Distribution of temperatures at $z = 3$ following reionization including RT (solid line) versus reionization in the optically thin limit (dashed line).

ionizing photons by an intervening optically thick system at the He II photoelectric edge. While for optically thin reionization all the gas everywhere is exposed to the photoionizing background, allowing for RT will produce shadowed regions in the presence of sufficiently dense clumps of gas. Only after He II reionization completes will the regions be reheated by overlapping ionization fronts.

The increase in the peculiar velocity compared with the computation in the optically thin approximation is shown in Fig. 9 (right-hand panel). The differences are small, typically less than $1\,\mathrm{km\,s^{-1}}$ as shown in Fig. 10 (dashed curve), except near the most overdense structures, or behind overdense regions which shadow the incident radiation field and delay full helium reionization. The small magnitudes are in contrast to the peculiar velocity boosts induced by reionization compared with the non-reionization case, shown in the left-hand panel. Reionization itself induces sizeable peculiar velocities, typically $0.1 < \Delta v < 10\,\mathrm{km\,s^{-1}}$, throughout most of the overdense gas, as shown in Fig 9 (left-hand panel) and Fig. 10 (solid curve).

A comparison of the two panels in Fig. 5 shows that some of the dense gaseous clumps present in the run without He II reionization disperse when He II reionization is included, particularly in the complex filamentary regions in the lower half of the figure. The differential impact of He II reionization on the gas density of the IGM is shown in Fig. 11 (left-hand panel). Substantial changes are found, with a ∼30 per cent decrease in underdense regions as the increased pressure gradients resulting from the additional heat input drive gas out of the shallower potential wells. Enhancements are produced as well, with the density increasing by as much as 50 per cent in dense regions when helium reionization is included. These regions tend to trace the filamentary structure of the gas distribution, suggesting they are too hot to accrete as readily on to nearby haloes.

Allowing for He II reionization, but in the optically thin limit, produces a similar gas density field to that with RT, as shown in Fig. 11 (right-hand panel). Large differences, however, occur in the more complex density regions, with the RT case generally resulting in more completely evacuated underdense regions.

The gas motion following He II reionization also produces a change in the dark matter distribution, although at a much smaller level. As gas is driven out of filamentary structures, the reduced gravitational potential will result in the dark matter readjusting to a somewhat lower density, as shown in Fig. 12. The differences are small at $z = 3$, on the order of 1 per cent or less. By $z = 2$, however, the differences have grown to as high as 3 per cent, with coherent structures several comoving megaparsecs in scale showing underdensities. As shown in Fig. 13, most of the differences are accounted for in the optically thin limit, but not entirely, especially in complex density regions such as in the lower middle region of the figure. Large-scale simulations with multiple QSO sources are necessary to estimate the impact on the matter power spectrum $P(k)$, however the results here suggest reionization may perturb $P(k)$ by a few per cent on comoving scales $k > 0.5\,h\,\mathrm{Mpc^{-1}}$ by $z = 2$.

5 SPECTRAL SIGNATURES

To assess the impact of RT on the spectral signatures of the Lyα forest, spectra against a fictitious background source are drawn from the ENZO simulations with and without RT. The spectra are

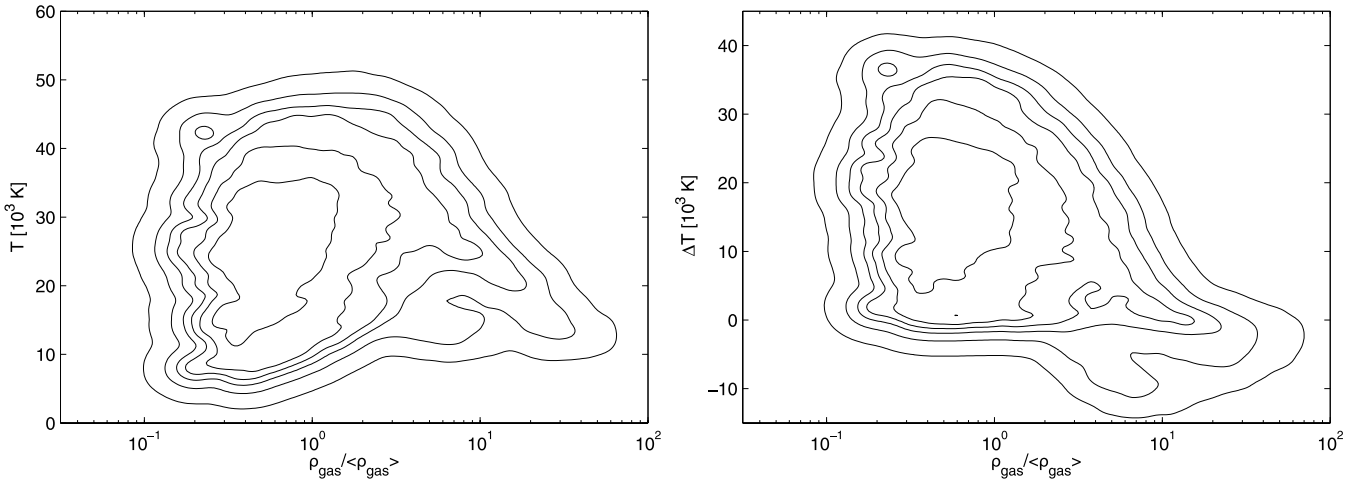

Figure 7. Left-hand panel: the temperature as a function of gas density at $z = 3.0$ following He II reionization including RT. Right-hand panel: the boost in temperature as a function of gas density at $z = 3.0$ including RT versus reionization in the optically thin limit. The contour levels are probability density levels (per $\mathrm{d}T - \mathrm{dlog}_{10}\rho/\langle\rho\rangle$) stepped by 0.5 dex starting at 10^{-7}.

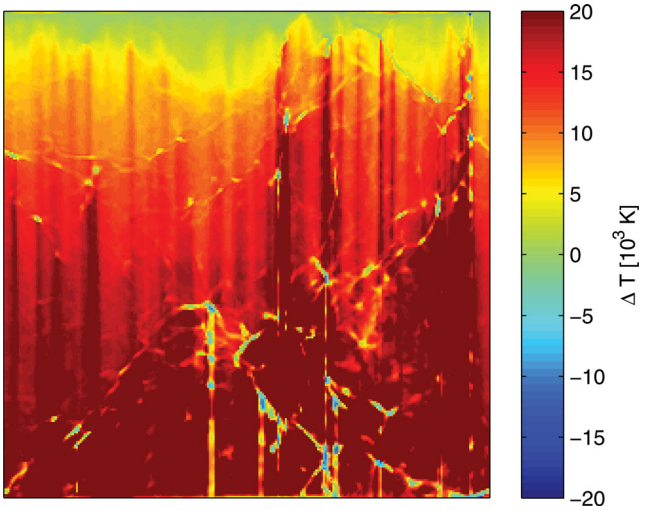

Figure 8. Map showing the change in the temperature including RT and without, at $z = 3.0$, following He II reionization. The box side is $25\,h^{-1}$ Mpc (comoving).

generated following the procedure described in Tittley & Meiksin (2007). They are constructed at an angle relative to the simulation axes in order to create a long non-repeating spectrum that wraps around a slice through the simulation volume. The velocity pixel widths are $5\,\mathrm{km\,s^{-1}}$. Both H I Lyα and He II Lyα spectra are made. The spectra are normalized to a mean transmission of $\langle\exp(-\tau)\rangle = \exp(-\tau_{\rm eff})$ with the values given in Table 2 for H I (Faucher-Giguère et al. 2008) and He II (Zheng et al. 2004b; Shull et al. 2010). Absorption lines are fitted to the spectra using AUTOVP (Davé et al. 1997), modified to recover from fatal errors (Meiksin et al. 2001). A signal-to-noise ratio of 100 is assumed for the fits. At $z = 3.0$, the He II Lyα transmission is very patchy and found too small to readily fit absorption line features.

5.1 H I absorption signature

The pixel flux distribution at $z = 3.0$ is shown following He II reionization both with and without RT in Fig. 14 (left-hand panels). Allowing for RT produces a smaller fraction of low optical depth pixels ($0.1 < \tau < 0.6$), and a larger fraction of very low values ($\tau < 0.1$), compared with the optically thin approximation (right-hand panels).

Also shown are the flux distributions recovered by fitting absorption lines to the spectra, and regenerating the flux distribution from the absorption lines alone. These are found to accurately recover the original flux distribution, demonstrating the absence of residual absorption that may not be accounted for by absorption lines.

The distribution of line centre optical depths is provided in the right-hand panels of Fig. 14, showing a higher fraction of lines with line centre optical depth $\tau_0 < 0.1$ for the case with RT compared with the optically thin limit. The higher proportion of very low fluctuations when RT is included may appear counter-intuitive since the temperatures, and so thermal pressures, are greater. The increased Jeans length may have been expected to smooth away small fluctuations in the spectra. Consideration of the dependence of the optical depth on the thermal width provides an explanation. Since the line centre optical depth varies as $\tau_0 \propto N_{\rm H\,I}/b$, for a given column density, an increased Doppler parameter due to heating the gas to a higher temperature reduces the line centre optical depth. The increase in temperature will also decrease the recombination rate at a given gas density, and so reduce the H I column density.

The column density and Doppler parameter distributions for the absorption line fits to the spectra are shown in Fig. 15. The column density distributions for the simulations with and without RT are very similar, with the distribution for the RT case somewhat broader. By contrast, the Doppler parameter distribution for the RT case shows a higher cut-off at the low end compared with the optically thin case. Dividing the lines into those optically thin and optically thick at line centre reveals that a large contribution to the offset originates from the optically thin lines. The median Doppler parameter of the optically thin absorption lines for the RT case is $b_{\rm med} \simeq 45\,\mathrm{km\,s^{-1}}$, while for the optically thin case, $b_{\rm med} \simeq 41\,\mathrm{km\,s^{-1}}$. For the optically thick absorbers, $b_{\rm med} \simeq 26\,\mathrm{km\,s^{-1}}$ for the RT case, while for the optically thin reionization case $b_{\rm med} \simeq 24\,\mathrm{km\,s^{-1}}$. Since the optically thin absorbers arise in moderate to low overdensity structures, the gas in the optically thin systems is too rarefied to establish thermal balance between radiative

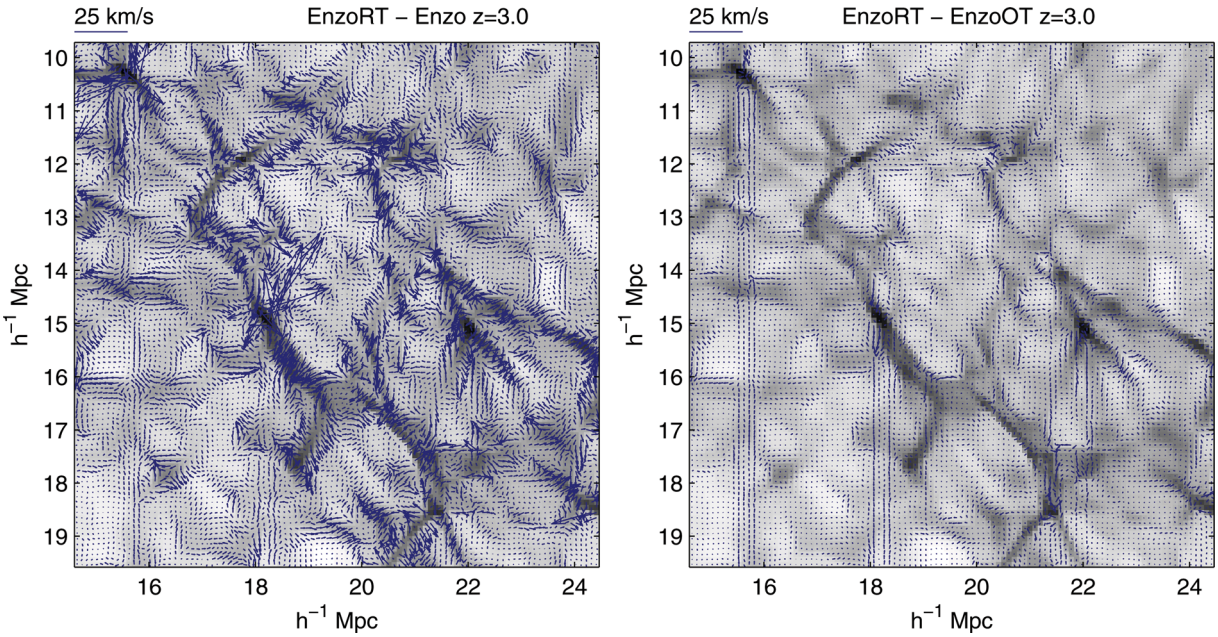

Figure 9. Differential peculiar velocity map in a kinematically complex region at $z = 3.0$. (The indicated box length scale is comoving.) Left-hand panel: map showing the change in the projected peculiar velocity of the gas with He II reionization including RT from the case without He II reionization. Right-hand panel: map showing the change in the projected peculiar velocity with He II reionization including RT from the case with He II reionization in the optically thin approximation.

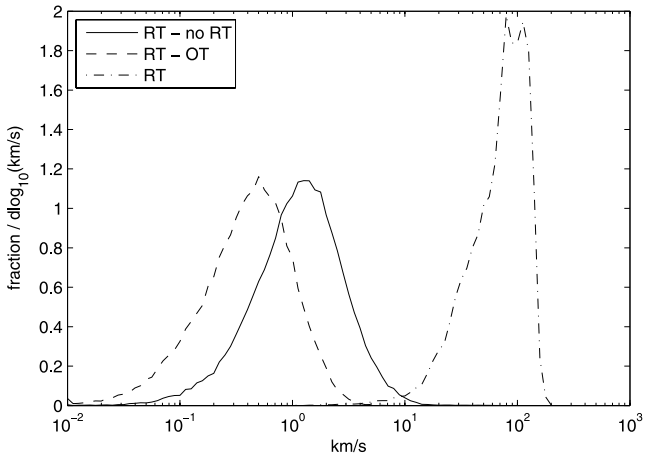

Figure 10. Distribution of peculiar velocity difference at $z = 3$ for reionization including RT versus the case with no reionization (solid line) and reionization in the optically thin limit (dashed line). Also shown is the total peculiar velocity distribution for the reionization simulation including RT (dot–dashed line).

heating and atomic cooling. As a consequence, the systems are overheated (Meiksin 1994; Miralda-Escudé & Rees 1994; Meiksin et al. 2001).

A similar trend was found for the optically thin reionization models of Meiksin et al. (2001) compared with the data: the median Doppler parameter of the measured optically thin lines was larger than for the lines drawn from the best-fitting ΛCDM model simulation. The median Doppler parameter for lines with $\tau_0 < 1$ measured in the spectrum of Q1937–1009 (Burles & Tytler 1997), over the redshift range $3.1 < z < 3.7$ was found to be $b_{\rm med} \simeq 29\,{\rm km\,s^{-1}}$, while the best-fitting model[2] gave $b_{\rm med} \simeq 20\,{\rm km\,s^{-1}}$. The measured median value for the systems with $\tau_0 < 1$ is substantially smaller than found here for the RT simulation, suggesting the He II reionization was too recent in the simulation (cf. Tittley & Meiksin 2007; Meiksin, Tittley & Brown 2010), or that the input spectrum was too hard on average. By contrast, the data for the $\tau_0 > 1$ systems gave $b_{\rm med} \simeq 26\,{\rm km\,s^{-1}}$, in agreement with the RT simulation result found here. A fully fair comparison with the observations, however, would require replicating the redshift range, resolution and noise properties of the measured spectra, as well as varying the luminosities, spectral shapes and timings of the sources. Such a comparison would require a large suite of simulations, which is not the purpose of this paper.

The evolution of the Doppler parameter cumulative distribution is shown in Fig. 16. The distributions show little evolution over $2.5 < z < 3.5$, but a marked decrease in the Doppler parameters by $z = 2.0$ as the IGM adiabatically cools following He II reionization. Dividing the absorption lines into those optically thick and thin at line centre (bottom panel) reveals that the optically thick systems undergo continual evolution towards smaller values with cosmic time, with the median Doppler parameter evolving from $b_{\rm med} \simeq 33\,{\rm km\,s^{-1}}$ at $z = 3.5$ to $19\,{\rm km\,s^{-1}}$ by $z = 2.0$ as the gas establishes thermal balance following He II reionization. By contrast, the systems optically thin at line centre show almost no evolution between $z = 3.5$ and 3.0, with heavily broadened lines following He II reionization having a median Doppler parameter $b_{\rm med} \simeq 44\,{\rm km\,s^{-1}}$, diminishing slightly to $39\,{\rm km\,s^{-1}}$ at $z = 2.5$, and then substantially to $27\,{\rm km\,s^{-1}}$ by $z = 2.0$.

[2] Both the simulated data and measured data were fitted using AUTOVP, with the redshift range, resolution and noise properties of the measured spectra duplicated in the simulated spectra.

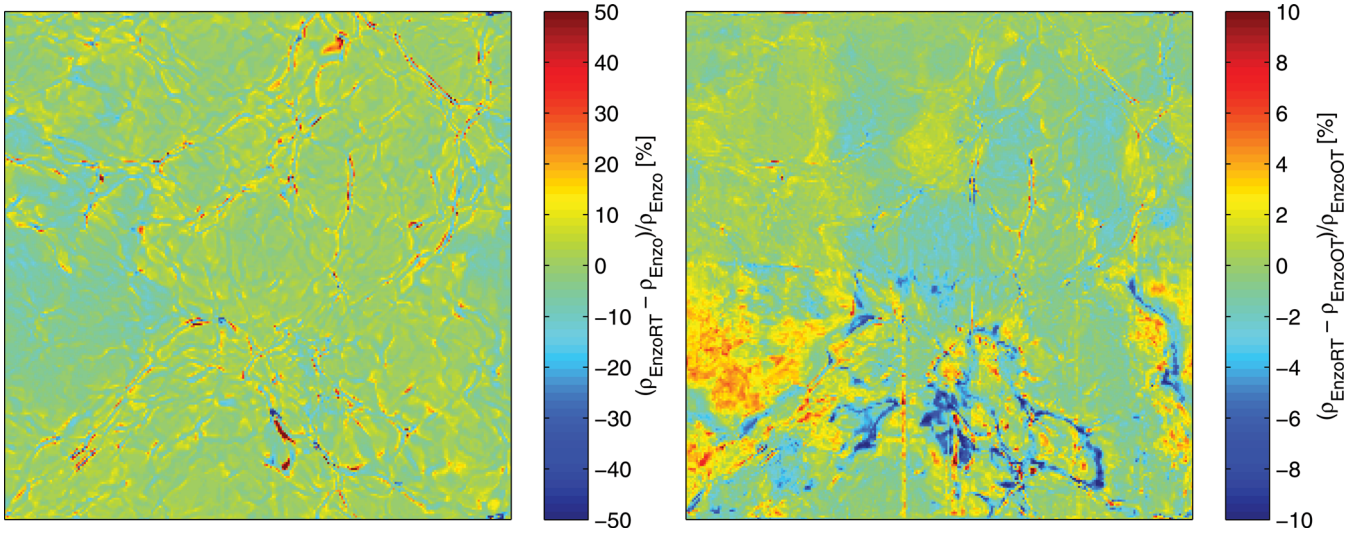

Figure 11. Maps showing the differential effect of He II reionization on the gas density at $z = 3$. Left-hand panel: map showing the percentage change in the gas density with He II reionization including RT from the case without He II reionization. Right-hand panel: map showing the percentage change in the gas density with He II reionization including RT from the case with He II reionization in the optically thin approximation. (Note change in scale.) The box side is $25h^{-1}$ Mpc (comoving).

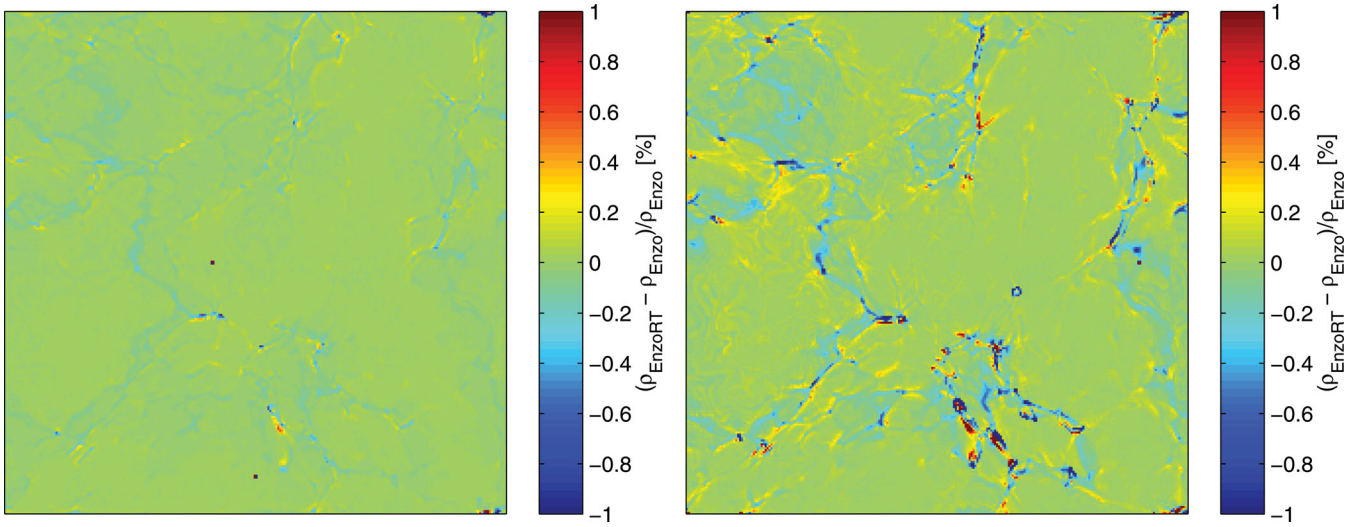

Figure 12. Maps showing the differential effect of He II reionization on the dark matter density at $z = 3$ (left-hand panel) and $z = 2$ (right-hand panel). The box side is $25h^{-1}$ Mpc (comoving).

In addition to the scattering of Lyα photons, the higher order Lyman resonance line photons will be scattered as well. Identifying individual absorption features in spectra is difficult except for the strongest lines, especially at high redshifts. The effective optical depths resulting from line blanketing, however, may be inferred. The observed effective optical depth at redshift z due to systems with rest-frame equivalent widths w (in wavelength units) is given by

$$\tau_{\rm l,Ly}n = \frac{1+z}{\lambda_{1n}} \int {\rm d}w \frac{\partial^2 N}{\partial z \partial w} w, \tag{11}$$

where λ_{1n} is the wavelength of the Lyman resonance line transition to the nth principal quantum level, and where the equivalent width is related to the line centre optical depth $\tau_{0,1n}$ by $w = 2(b/c)\lambda_{1n}F(\tau_{0,1n})$, where $F(\tau)$ is a function dependent on the Voigt profile (Meiksin 2009). If the line distribution is separable into the form $\partial^2 N/\partial z \partial w = ({\rm d}N/{\rm d}z) f(w/w^*_{1n})$, where the equivalent width distribution $f(w/w^*_{1n})$ may be characterized by a single parameter w^*_{1n}, such as the scale height for an exponential distribution $f(w/w^*_{1n}) = \exp(-w/w^*_{1n})$, then the effective optical depths for transitions to levels n and n' are related by

$$\frac{\tau_{\rm l,}n'}{\tau_{\rm l,}n} = \frac{F\left(\frac{\lambda_{1n'} f_{1n'}}{\lambda_{1n} f_{1n}} \tau^*_{0,1n}\right)}{F(\tau^*_{0,1n})}, \tag{12}$$

where $\tau^*_{0,1n}$ is given by $w^*_{1n} = 2(b/c)\lambda_{1n}F(\tau^*_{0,1n})$.

The ratios $\tau_{\rm l,Ly}\beta/\tau_{\rm l,Ly}\alpha$ and $\tau_{\rm l,Ly}\gamma/\tau_{\rm l,Ly}\alpha$ from the `EnzoRT` run are shown in the upper panel of Fig. 17. A rise in both ratios occurs at redshifts $z < 4$ once He II reionization begins. The inferred values of the characteristic Lyα optical depth $\tau^*_{\rm Ly}\alpha$ are shown in the bottom

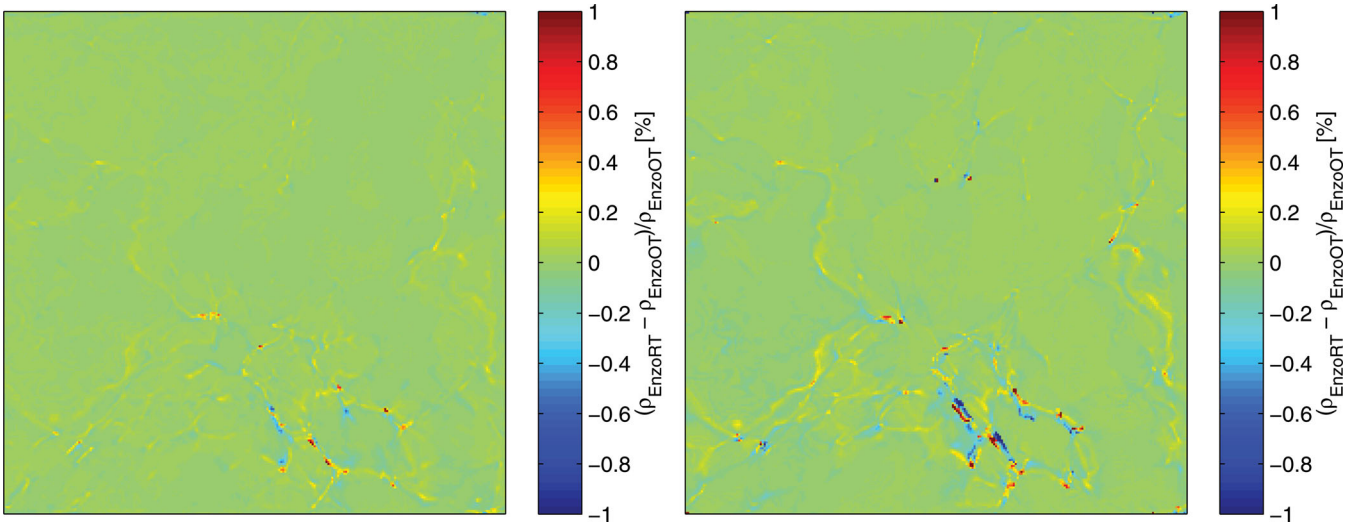

Figure 13. Maps showing the differential effect of He II reionization on the dark matter density allowing for full RT compared with He II reionization in the optically thin approximation. Shown at $z = 3$ (left-hand panel) and $z = 2$ (right-hand panel). The box side is $25h^{-1}$ Mpc (comoving).

Table 2. Effective IGM optical depths for H I and He II Lyα.

	z				
Component	2.0	2.5	3.0	3.5	4.0
$\tau_{\rm eff}^{\rm H\,I}$	0.13	0.23	0.40	0.72	0.89
$\tau_{\rm eff}^{\rm He\,II}$	0.45	2.0	5.0	–	–

panel. The corresponding predicted values of $\tau_{\rm l,Ly\gamma}/\tau_{\rm l,Ly\alpha}$ (upper panel) lie close to, but somewhat below, the values measured from the simulation, suggesting the single parameter separable model for the line distribution provides a good description of the line blanketing, but becomes less accurate at large values of $\tau^*_{\rm Ly\alpha}$.

5.2 He II absorption signature

For a homogeneous radiation field, the ratio of the He II to H I optical depths per pixel is

$$\frac{\tau_{\rm He\,II}}{\tau_{\rm H\,I}} = \frac{1}{4}\frac{N_{\rm He\,II}}{N_{\rm H\,I}}\frac{b_{\rm H\,I}}{b_{\rm He\,II}}, \tag{13}$$

where $N_{\rm H\,I}$ and $N_{\rm He\,II}$ are the H I and He II column densities, respectively, and $b_{\rm H\,I}$ and $b_{\rm He\,II}$ the corresponding Doppler parameters. For pure thermal broadening, $b_{\rm He\,II} = b_{\rm H\,I}/2$, while for velocity-broadened lines, $b_{\rm He\,II} = b_{\rm H\,I}$. For metagalactic H I and He II photoionization rates $\Gamma_{\rm H\,I}$ and $\Gamma_{\rm He\,II}$, the column density ratio, for a hydrogen to helium number density ratio of 12.9, is

$$\begin{aligned}\frac{N_{\rm He\,II}}{N_{\rm H\,I}} &= \frac{\Gamma_{\rm H\,I}}{\Gamma_{\rm He\,II}}\frac{n_{\rm He}}{n_{\rm H}}\frac{\alpha_{\rm He\,III}}{\alpha_{\rm H\,I}} \\ &\simeq 0.31\frac{\Gamma_{\rm H\,I}}{\Gamma_{\rm He\,II}}\frac{7.107 - (1/2)\log T + 0.00547T^{1/3}}{6.414 - (1/2)\log T + 0.00868T^{1/3}} \\ &\simeq 0.42\frac{\Gamma_{\rm H\,I}}{\Gamma_{\rm He\,II}},\end{aligned} \tag{14}$$

where the last form is accurate to 5 per cent for $10^4 < T < 5 \times 10^4$ K (Madau & Meiksin 1994; Meiksin 2009). The optical depth ratio is thus a measure of the fluctuations in the ratio of the radiation field as well as the velocity broadening of the absorption lines.

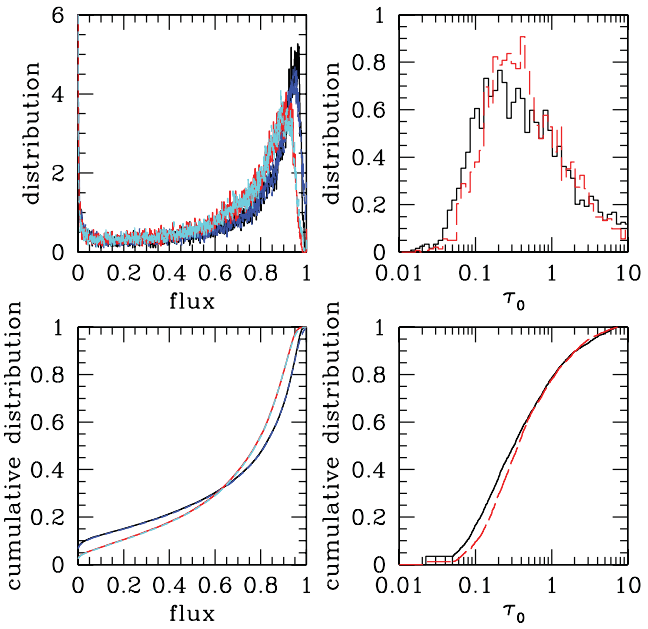

Figure 14. Top-left panel: the pixel flux distribution functions at $z = 3$ following He II reionization for ENZO with RT (black solid line) and in the optically thin limit (red solid line). Also shown is the recovery of the flux distributions using only the fit absorption features for the run with RT (blue short-dashed line) and without (cyan short-dashed line). Bottom-left panel: the corresponding cumulative flux distributions. Top-right panel: the distributions of line centre optical depth for the fit lines for reionization including RT (black solid line) and without (red long-dashed line). Bottom-right panel: the corresponding cumulative distributions.

The distribution of the optical depth ratio per pixel is shown in Fig. 18 for $2 < z < 3$. The distributions show a wide range of values, with the peak declining from 105 at $z = 3$ to 75 at $z = 2$. The full width at half-maximum (FWHM) of the distributions is about 20–30, changing little with redshift. The variations arise entirely from

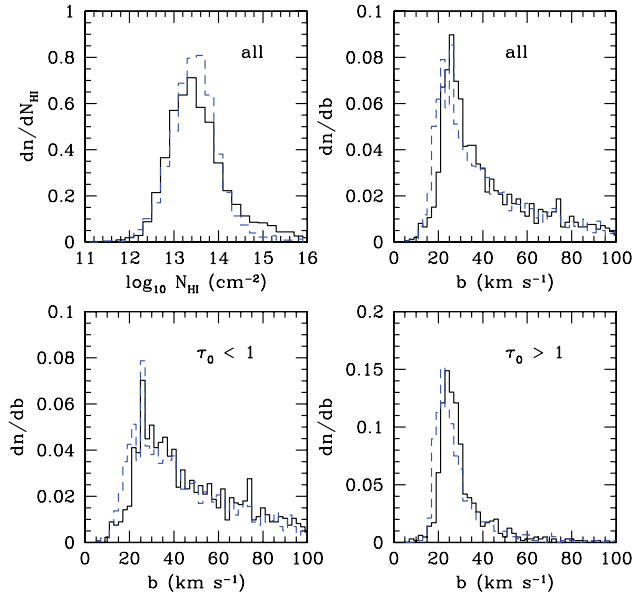

Figure 15. Top-left panel: the H I column density distributions at $z = 3$ following He II reionization for EnzoRT (solid line; black) and in the optically thin limit (dashed line; blue). Top-right panel: the corresponding Doppler parameter distributions. Lower-left panel: the Doppler parameter distributions for absorption lines with line centre optical depth $\tau_0 < 1$. Lower-right panel: the Doppler parameter distributions for absorption lines with $\tau_0 > 1$.

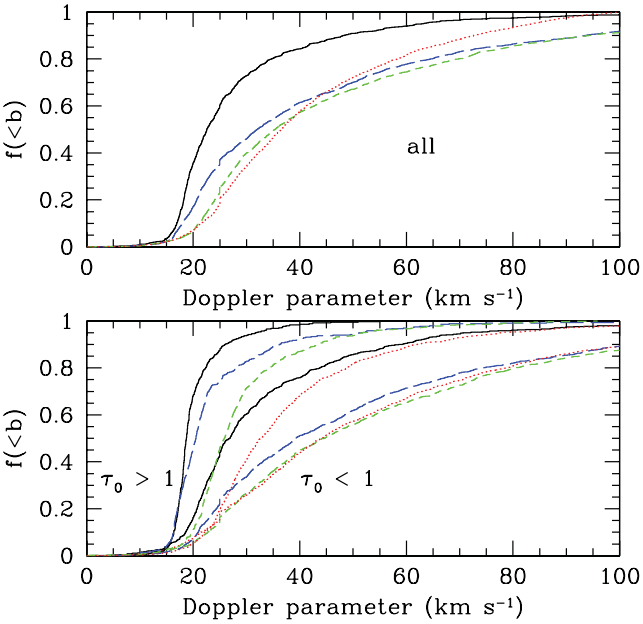

Figure 16. Top panel: the H I Doppler parameter cumulative distribution for EnzoRT, shown at $z = 2$ (solid line; black), 2.5 (long-dashed line; blue), 3.0 (short-dashed line; green) and 3.5 (dotted line; red). Bottom panel: as in the top panel, but with the lines divided between those with line centre optical depth $\tau_0 < 1$ (rightmost curves) and those with $\tau_0 > 1$ (leftmost curves).

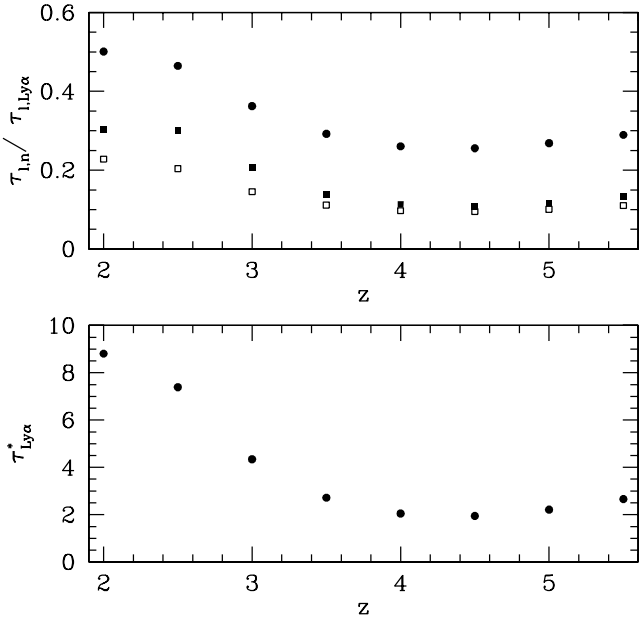

Figure 17. Top panel: the ratios of the effective optical depths $\tau_{1,Ly\beta}/\tau_{1,Ly\alpha}$ (solid points) and $\tau_{1,Ly\gamma}/\tau_{1,Ly\alpha}$ (solid squares) for H I obtained from the EnzoRT run, as a function of redshift z. Also shown is the predicted ratio $\tau_{1,Ly\gamma}/\tau_{1,Ly\alpha}$ (open squares) based on a line-blanketing model (see text). Bottom panel: the characteristic H I $\tau^*_{Ly\alpha}$ optical depth inferred from the values of $\tau_{1,Ly\beta}/\tau_{1,Ly\alpha}$ from the EnzoRT run.

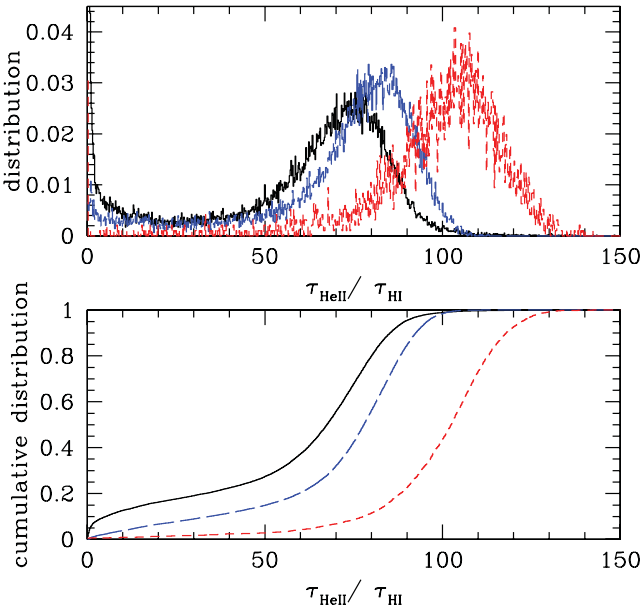

Figure 18. Top panel: the distributions of the ratio of the pixel optical depths $\tau_{He\,II}/\tau_{H\,I}$ in the spectra following He II reionization for EnzoRT at $z = 2.0$ (solid line; black), 2.5 (long-dashed line; blue) and 3.0 (short-dashed line; red). Bottom panel: the corresponding cumulative distributions.

the RT of the incident radiation through an inhomogeneous medium following helium reionization. Allowing for the Poisson fluctuations from the finite number of sources within an attenuation volume for He II ionizing photons will further enhance the fluctuations (Fardal et al. 1998; Bolton et al. 2006; Meiksin 2009; Furlanetto & Dixon 2010).

Absorption lines were fitted in the He II spectrum at $z = 2.5$. To facilitate comparison with the published results, the He II spectra were renormalized to an effective optical depth of $\tau_{\rm eff}^{\rm He\,II} = 0.74$, the value measured by Fechner et al. (2006) at $z \simeq 2.45$. The He II

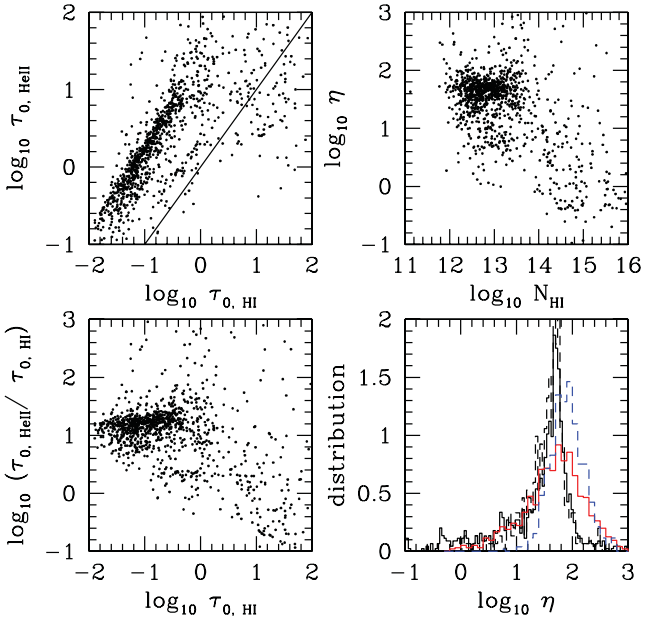

Figure 19. Comparison of EnzoRT results for H I and He II line centre optical depths and column densities for fit absorption features at $z = 2.5$. Top-left panel: comparison of line centre optical depths for H I and He II absorption features. The solid line shows the relation $\tau_{0,\mathrm{He\,II}} = \tau_{0,\mathrm{H\,I}}$. Bottom-left panel: He II to H I line centre optical depth ratio versus H I line centre optical depth. Top-right panel: He II to H I column density ratio η versus H I column density. Bottom-right panel: distribution functions of η for all lines (solid black histogram), and lines restricted to $0.01 < \tau_{0,\mathrm{H\,I}} < 0.1$ (dashed black histogram). Also shown are the distribution functions for HS 1700+6416 (Fechner et al. 2006) for absorption features in the redshift range $2.29 \lesssim z \lesssim 2.75$ for all the lines (solid red histogram) and for lines restricted to $0.01 < \tau_{0,\mathrm{H\,I}} < 0.1$ (blue dashed histogram). All distribution functions are normalized to unit area. The He II spectra were renormalized to $\tau_{\mathrm{eff}}^{\mathrm{He\,II}} = 0.74$ to match the value measured by Fechner et al. (2006).

absorption features were matched to the H I features, requiring a line centre velocity difference smaller than $10\,\mathrm{km\,s^{-1}}$ for a successful match. The relation between the matching line centre optical depths is shown in Fig. 19. While the deblending of absorption features will introduce scatter into the relation, a clear correlation is apparent in the left-hand panels corresponding to $\tau_{0,\mathrm{He\,II}}/\tau_{0,\mathrm{H\,I}} \lesssim 15$. For weak H I lines, the ratio is found to increase slightly towards increasing $\tau_{0,\mathrm{H\,I}}$ (lower-left panel). For saturated H I features, however, the ratio decreases with increasing line centre optical depth. A similar trend was found for simulated spectra for absorption lines in the redshift range $2.29 \lesssim z \lesssim 2.75$ by Fechner et al. (2006), who argued the correlation was a spurious artefact of the line fitting and that statistically meaningful comparisons must be restricted to systems with $\tau_{0,\mathrm{H\,I}} < 0.1$.

The distribution of column density ratios $\eta = N_{\mathrm{He\,II}}/N_{\mathrm{H\,I}}$ in Fig. 19 shows a similar decreasing trend towards increasing $N_{\mathrm{H\,I}}$ (top-right panel). A broad distribution of η values for all the systems is found (lower-right panel). Restricting the systems to those with $0.01 < \tau_{0,\mathrm{H\,I}} < 0.1$, however, results in a far sharper distribution centred at $\eta \simeq 53$. Combining with the median ratio of $\tau_{0,\mathrm{He\,II}}/\tau_{0,\mathrm{H\,I}}$, equation (13) indicates a typical Doppler parameter ratio of $b_{\mathrm{He\,II}}/b_{\mathrm{H\,I}} \simeq 0.9$. The peak and FWHM in the distribution of η at $z = 2.5$ from the simulation correspond to an effective $\Psi = \Gamma_{\mathrm{H\,I}}/\Gamma_{\mathrm{He\,II}} \simeq 125^{+25}_{-42}$. The modification of Ψ within the simulation produced by RT is found to be highly inhomogeneous, with typically 40–60 per cent variations produced in the He II ionization rate during the passage of the He III ionization front. The larger values of Ψ are comparable to those inferred from observations (Zheng et al. 2004b; Reimers et al. 2005; Fechner et al. 2006; Shull et al. 2010).

The η distributions are similar in shape to those measured (Fechner et al. 2006), with the distribution for systems restricted to $0.01 < \tau_{0,\mathrm{H\,I}} < 0.1$ peaking at $\eta \lesssim 90$ and somewhat broader than the distribution found from EnzoRT. For comparison, the unrestricted measured distribution peaks at $\eta \simeq 55$, while the simulated at $\eta \simeq 48$. As discussed below in connection with an optically thin ENZO simulation, the peak in the distribution for the EnzoRT simulation results both from the normalizations imposed on the effective H I and He II optical depths and the effects of RT. The mean and width of the measured distribution may be reproduced by Poisson fluctuations in the expected QSO numbers within a He II ionizing photon attenuation volume in a homogeneous IGM (Meiksin 2009). The results found here suggest a comparable width to the distribution could instead arise from RT effects following He II reionization by a single ionization front, the source for which by $z = 2.5$ has transformed entirely into a QSO-like power-law spectrum. However, as the hydrogen ionization field, as for the helium, is produced by the flux incident on a single side of the simulation volume, shadowing of both hydrogen and helium ionizing radiation will be present. While the hydrogen ionization rate inferred from observations may be accounted for fully by QSO sources at $z \leq 2.5$ (Meiksin & White 2004), the attenuation volume of hydrogen-ionizing photons is expected to be sufficiently large to contain at least hundreds of QSOs, so that there should be little fluctuation in the H I ionizing background. In particular, the tail of low η values for the sample unrestricted in $\tau_{0,\mathrm{H\,I}}$ in Fig. 19 would be absent, as it arises predominantly from a few shadowed regions in which the H I ionizing radiation field is more strongly attenuated than the He II. A fairer comparison with the fluctuations in η would require imposing a uniform H I ionizing background on the simulation volume after H I re-ionization completes.

The relation between the H I and He II Doppler parameters for the absorption systems at $z = 2.5$ is shown in Fig. 20. The H I absorption lines are restricted to those with $0.01 < \tau_{0,\mathrm{H\,I}} < 0.1$. In the limit of pure thermal broadening, the He II to H I ion mass ratio would result in He II systems with $\xi = b_{\mathrm{He\,II}}/b_{\mathrm{H\,I}} = 1/2$. In the limit of velocity broadened lines, $\xi = 1$. The upper-left panels show that the Doppler parameters lie predominantly between these two limiting cases. Many of the points lie outside the limiting cases, a consequence of fitting lines to blended features as well as to saturated He II features. The wide scatter suggests the Doppler parameter ratio ξ is not a precise indicator of the relative contributions to line broadening due to thermal motions and internal flows. Similar results were found for selected unblended absorption systems in the spectrum of HE 2347−4342 in the redshift range $2.7 < z < 2.8$, although the ratios tended more towards velocity broadening than thermal (Zheng et al. 2004b). No strong correlation is found between ξ and $N_{\mathrm{H\,I}}$ (top-right panel), however the ratio tends to increase with increasing η (bottom-right panel), although this may be an effect of line deblending by the fitting algorithm.

The ratios $\tau_{1,\mathrm{Ly}\beta}/\tau_{1,\mathrm{Ly}\alpha}$ and $\tau_{1,\mathrm{Ly}\gamma}/\tau_{1,\mathrm{Ly}\alpha}$ for He II from the EnzoRT simulation after reionization completes at $z \leq 3$ are shown in the upper panel of Fig. 21, renormalizing the spectra by $\tau_{1,\mathrm{Ly}\alpha}$ to the values indicated. In the region of overlap, these values agree with the simulation results quoted in Syphers et al. (2011b). The inferred effective line centre optical depths $\tau^{*}_{0,\mathrm{Ly}\alpha}$ using equation (12) are shown in the lower panel. The resulting predicted values for $\tau_{1,\mathrm{Ly}\gamma}/\tau_{1,\mathrm{Ly}\alpha}$ from equation (12) are shown by the dotted line in the upper panel. The

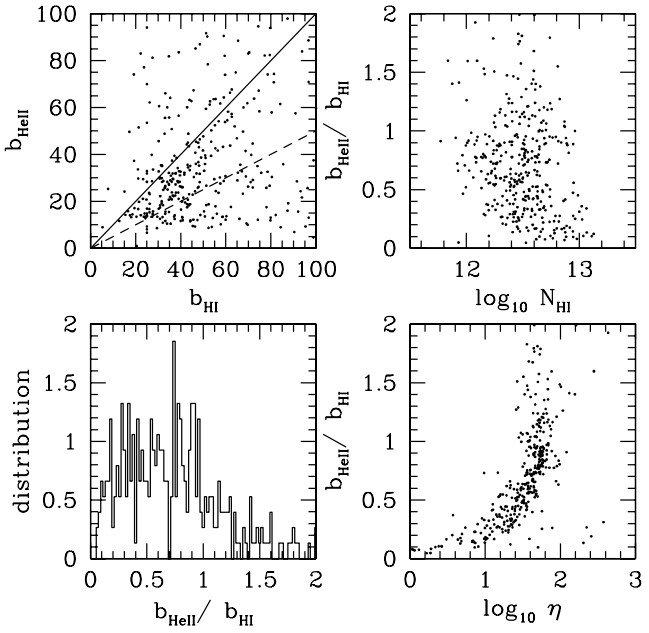

Figure 20. Comparison of EnzoRT results for H I and He II Doppler parameters for fit absorption features at $z = 2.5$ with $0.01 < \tau_{0,\mathrm{H\,I}} < 0.1$. Top-left panel: comparison of $b_{\mathrm{H\,I}}$ and $b_{\mathrm{He\,II}}$ absorption features. The solid line shows the relation for pure velocity broadening; the dashed line shows the relation for pure thermal broadening. Bottom-left panel: the distribution function of $b_{\mathrm{He\,II}}/b_{\mathrm{H\,I}}$. Top-right panel: Doppler parameter ratio versus H I column density. Bottom-right panel: Doppler parameter ratio versus He II to H I column density ratio η. The He II spectra were renormalized to $\tau_{\mathrm{eff}}^{\mathrm{He\,II}} = 0.74$ to match the value measured by Fechner et al. (2006).

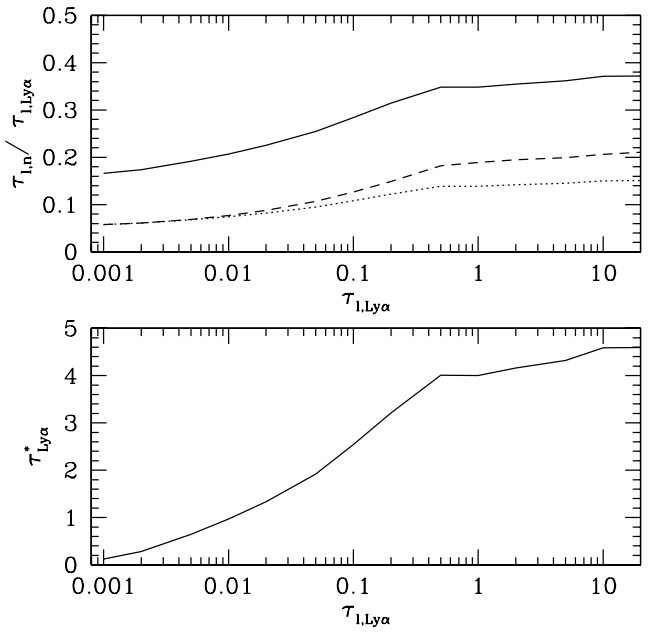

Figure 21. Top panel: the ratios of the effective optical depths $\tau_{\mathrm{l,Ly}\beta}/\tau_{\mathrm{l,Ly}\alpha}$ (solid line) and $\tau_{\mathrm{l,Ly}\gamma}/\tau_{\mathrm{l,Ly}\alpha}$ (dashed line) for He II obtained from the EnzoRT run, as a function of $\tau_{\mathrm{l,Ly}\alpha}$. (The result is insensitive to redshift after reionization completes at $z \leq 3$.) Also shown is the predicted ratio $\tau_{\mathrm{l,Ly}\gamma}/\tau_{\mathrm{l,Ly}\alpha}$ (dotted line) based on a line-blanketing model (see text). Bottom panel: the characteristic He II $\tau^*_{\mathrm{Ly}\alpha}$ optical depth inferred from the values of $\tau_{\mathrm{l,Ly}\beta}/\tau_{\mathrm{l,Ly}\alpha}$ from EnzoRT.

values agree well with those measured directly from the simulation, indicating the absorption is well described by the line model, although the small deviation for large optical depths suggests the simple one-parameter model only approximately describes the underlying distribution at these large optical depths.

For comparison, the value measured in the QSO HE 2347−4342 ($z_{\mathrm{em}} \simeq 2.89$), with $\tau^{\mathrm{eff}}_{\mathrm{Ly}\alpha} \simeq 2.393 \pm 0.015$ at $\langle z \rangle \simeq 2.8$, is $\tau^{\mathrm{eff}}_{\mathrm{Ly}\beta}/\tau^{\mathrm{eff}}_{\mathrm{Ly}\alpha} \simeq 0.31 \pm 0.04$, using the data from Syphers et al. (2011b). This agrees well with the value of $\tau_{\mathrm{l,Ly}\beta}/\tau_{\mathrm{l,Ly}\alpha} \simeq 0.36$ predicted from the EnzoRT simulation, as shown in Fig. 21.

6 COMPARISON WITH APPROXIMATE METHODS

6.1 Approximate methods

Two approximate simulation methods have been used in the past to characterize the effects of He II reionization on the IGM. One method uses *N*-body code results to represent the fluid by rescaling the dark matter density (Tittley & Meiksin 2007; McQuinn et al. 2009); it thus does not account for the hydrodynamical response of the gas to heating due to RT. A similar method post-processes hydrodynamical simulations using a RT module, but also does not include the hydrodynamical response of the gas to the RT (Bolton & Haehnelt 2007). An alternative method artificially boosts the He II heating rates in optically thin gravity-hydrodynamics reionization simulations to mimic the boost in temperatures resulting from RT effects (Bryan & Machacek 2000).

To estimate the importance of hydrodynamical feedback effects on the observed properties of the Lyα forest, we compare the results of the hydrodynamics simulations including RT with the results of the *N*-body RT code PMRT (Tittley & Meiksin 2007). PMRT assumes the baryons trace the dark matter. The code is thus not able to cope with sudden increases in the pressure forces as the gas is heated and driven out of shallow potential wells or heated by shocks in collapsing structures.

Past comparisons with full hydrodynamics computations without RT show that the method recovers the distribution of Doppler parameters to high accuracy, although the median Doppler parameter may be slightly broadened by 1–2 km s^{-1} (Meiksin & White 2001). A pseudo-hydrodynamics scheme with RT has the advantages over a fully hydrodynamical one of ease of implementation and a much reduced memory requirement, permitting simulations in larger boxes at the high spatial resolution required to resolve the structures in the IGM that give rise to the full range of measurable absorption systems. Here we examine how successful PMRT simulations are at capturing the essential features of the Lyα forest predicted by full hydrodynamics computations including RT.

The PMRT runs used 512^3 gravitating particles, with the identical initial particle distributions in position and velocity as for the ENZO runs, and the identical cosmological parameters. It used the identical RT module as for the ENZO runs, using 256^3 cells to represent the fluid. Following Tittley & Meiksin (2007), all cells with fewer than 100 particles were convolved over a radius of 1.5 cells to match the gas distribution from ENZO.

We also implement the alternative method of artificially boosting the He II heating rate in a hydrodynamical simulation in the optically thin limit to make up for the shortfall in the additional heating due to RT effects. A boost by a factor of 2 was found to provide sufficient heat to broaden the absorption lines close to the measured values at $z \simeq 3$ (Bryan & Machacek 2000). We recompute the reionization

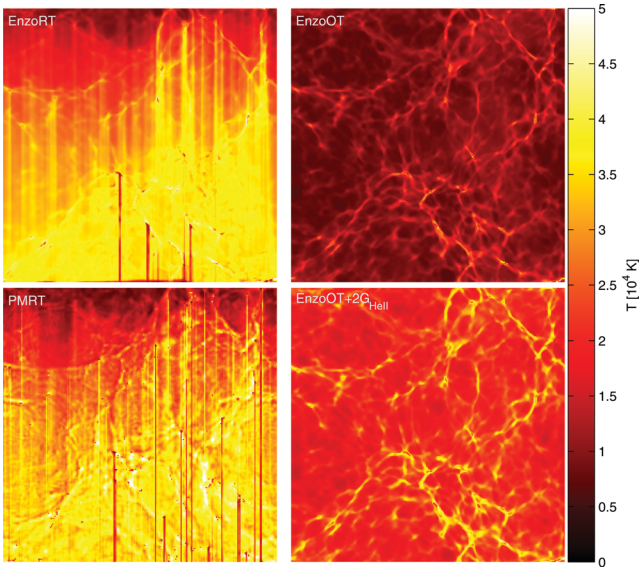

Figure 22. Temperature map at $z = 3.3$, shortly before He II reionization completes. The ionization front sweeps across the boxes from top to bottom. The maps are shown for `EnzoRT` (upper left), `EnzoOT` (upper right), `EnzoOT`+$2G_{\rm He\,II}$ (lower right) and `PMRT` (lower left). The box side is $25\,h^{-1}$ Mpc (comoving).

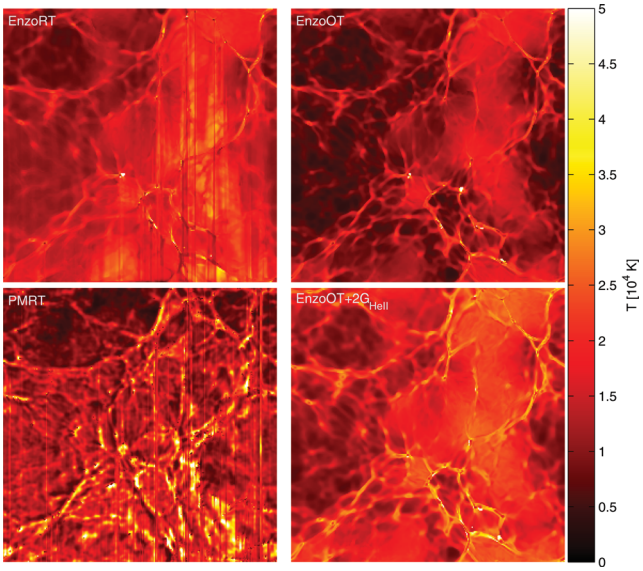

Figure 23. Temperature map at $z = 2.0$, well after He II reionization completes. The ionization front swept across the boxes from top to bottom. The maps are shown for `EnzoRT` (upper left), `EnzoOT` (upper right), `EnzoOT`+$2G_{\rm He\,II}$ (lower right) and `PMRT` (lower left). The box side is $25\,h^{-1}$ Mpc (comoving).

simulation using ENZO with the He II heating rate per He II ion boosted to $G'_{\rm He\,II} = 2G_{\rm He\,II}$, and the RT switched off.

6.2 Physical properties of the IGM

Maps of the IGM temperature are shown in Fig. 22 at $z = 3.3$, shortly before He II reionization completes, and in Fig. 23 at $z = 2$, well after completion. At $z = 3.3$, the `PMRT` run matches most closely to the `EnzoRT` simulation. There are, however, some conspicuous differences. The temperature structures tend to be sharper in the `PMRT` simulation, as it lacks both shock heating and the pressure forces that smooth the gas. The effect of shadowing by dense clumps is also more prevalent in the `PMRT` simulation. This is a consequence of the inability of the dense regions to expand due to pressure forces as the ionization front sweeps across and boosts the gas temperature and pressure, as discussed in Section 4.2. The ENZO simulation with the boosted He II heating rate recovers the high temperatures in the filaments, but the temperatures in the underdense regions, although warmer than in the optically thin simulation, still lie well below the ENZO simulation with RT.

By $z = 2.0$, the `PMRT` simulation shows significant discrepancies in the gas temperature within the filaments compared with the `EnzoRT` simulation. In contrast to the hydrodynamics simulation which accounts for the hydrodynamical response of the gas to the extra heating following He II reionization, allowing it to expand and cool, the `PMRT` simulation keeps the gas too hot. In underdense regions, the `PMRT` simulation overestimates the amount of adiabatic cooling, resulting in the gas becoming too cold. The ENZO simulation with the boosted He II heating rate is better able to reproduce the temperatures in the underdense regions, but maintains the gas in the filaments at too high temperatures compared with the `EnzoRT` simulation.

These effects may be quantified using the temperature–density distributions extracted from the simulations. The temperature–density distribution obtained from the `PMRT` run closely resembles that found for `EnzoRT` at $z \geq 3.0$, as shown in Fig. 24, with reasonably good agreement down to $z = 2$. The distributions overlap very closely, although the hydrodynamics computation shows a somewhat tighter and flatter distribution in temperatures, especially towards $z = 2$. While the temperatures in the optically thin simulation with boosted He II heating rate agree well with the RT simulations for $\rho/\langle\rho\rangle > 3$ over $3.0 \leq z \leq 3.5$, the temperatures are appreciably

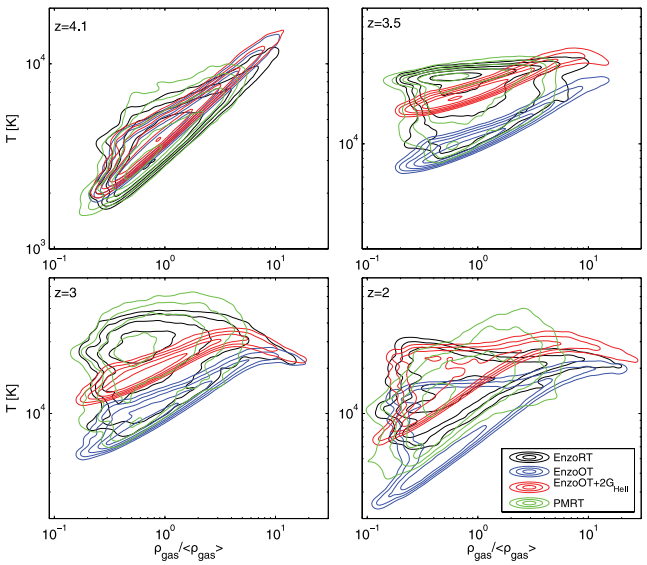

Figure 24. Temperature–density distributions at $z = 4.1$, 3.5, 3.0 and 2.0 following He II reionization, for computation using ENZO with RT, ENZO in the optically thin limit, ENZO in the optically thin limit but with the He II heating rate doubled, and the pseudo-hydrodynamics RT run `PMRT`. Note the smaller temperature scale at $z = 4.1$, prior to He II reionization. The distributions are normalized to unity. The contour levels are at probability density levels (per $\mathrm{dlog}_{10}T - \mathrm{dlog}_{10}\rho/\langle\rho\rangle$) 0.1, 0.32, 1.0, 3.2, 10, 32, ...

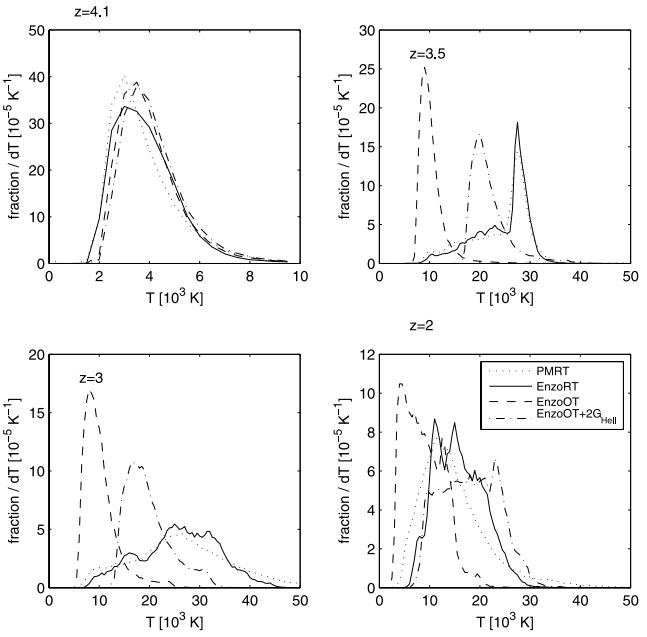

Figure 25. Temperature distributions at $z = 4.1$, 3.5, 3.0 and 2.0 for computation using ENZO with RT (solid lines), ENZO in the optically thin limit (dashed lines), ENZO in the optically thin limit but with the He II heating rate doubled (dot–dashed lines) and the pseudo-hydrodynamics RT run PMRT (dotted lines). Note the smaller temperature scale at $z = 4.1$, prior to He II reionization.

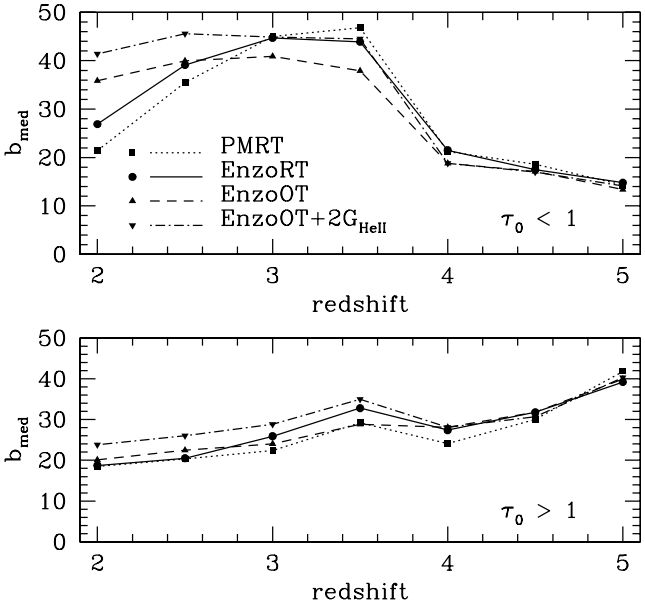

Figure 26. Evolution in the median Doppler parameter for the computation using ENZO with RT (solid lines), ENZO in the optically thin limit (dashed lines), ENZO in the optically thin limit with the He II heating rate doubled (dot–dashed lines) and the pseudo-hydrodynamics run PMRT (dotted lines). Top panel: results for lines optically thin at line centre. Bottom panel: results for lines optically thick at line centre.

lower in structures with $\rho/\langle\rho\rangle < 1$. At $z = 2$, good agreement is found for underdense structures between the EnzoRT run and the boosted He II heating rate simulations, but the latter produces too high temperatures for overdense structures. The distribution from the optically thin ENZO simulation agrees well with the others at $z = 4$, but once He II reionization commences, the temperatures are systematically too low.

The temperature distributions of the EnzoRT and PMRT runs are very similar, as shown in Fig. 25, which may be expected from the overall agreement in the density–temperature distributions. By $z = 2.0$, however, the PMRT simulation systematically underestimates the temperatures by 3–5 $\times$ 10^3 K. Most of the volume is too cold in the ENZO simulation with the boosted He II heating rate for $3.0 \leq z \leq 3.5$, although a tail of warmer temperatures results from overdense material, as shown in Fig. 24. By $z = 2$, these temperatures extend the distribution towards too high values compared with the RT simulations.

6.3 Spectral signatures

To assess the observational impact of the physical differences arising from the hydrodynamical response of the gas compared with the pseudo-hydrodynamics simulation on the Lyα forest, sample spectra are drawn from the ENZO and PMRT simulations, and the absorption features fit. As is clear from Figs 9 and 10, reionization induces substantial peculiar velocities to the gas that a pseudo-hydrodynamics scheme like PMRT is unable to reproduce. The differences are small compared with the peculiar velocities present due to large-scale flows, as is evident by a comparison with the full peculiar velocity distribution shown by the rightmost curve in Fig. 10. The comparison between the ENZO run with RT and the run without reionization, however, suggests differences as great as 10 km s^{-1} are produced, with differences of 1–2 km s^{-1} typical. These should be reflected in the line widths, although the differences in gas temperature will affect the line widths as well. For a pre-He II ionization temperature of 5000 K, a temperature boost to 20 000 K will double the thermal line width, increasing it to 18 km s^{-1}. The additional broadening due to the increase in peculiar velocity will augment the increase due to thermal broadening by at most only a few kilometres per second. In comparison with the optically thin reionization simulation, the additional peculiar velocities induced when RT is included add negligibly to the broadening.

The evolution of the resulting median Doppler parameters is shown in Fig. 26. The values generally agree well for the absorption lines optically thick at the line centre (bottom panel), although with deviations of $\sim\pm4$ km s^{-1} from the EnzoRT simulation. The optically thin ENZO simulations agree best with the RT run at $z > 3$, with the simulations with the boosted and non-boosted He II heating rates bracketing the RT simulation, but producing too broad features by $z < 3$, where the PMRT simulation gives near perfect agreement.

By contrast, the PMRT simulation recovers the median Doppler parameters for the absorption lines optically thin at line centre for $z > 3$. These weaker lines arise from gas too rarefied to maintain atomic thermal balance with the photoionization heating rate, so that including the temperature heating due to RT is required. The good agreement with the EnzoRT simulation results shows that hydrodynamical feedback contributes little additional broadening to the lines. The optically thin ENZO simulation produces lines that are $\sim$5 km s^{-1} too narrow at $3 < z < 3.5$. Boosting the He II heating rate recovers the median Doppler parameter well for $3 < z < 3.5$, but overheats the gas at lower redshifts. At $z < 3$, adiabatic cooling in the PMRT simulation produces features that are too narrow compared with the EnzoRT simulation. None of the approximate methods

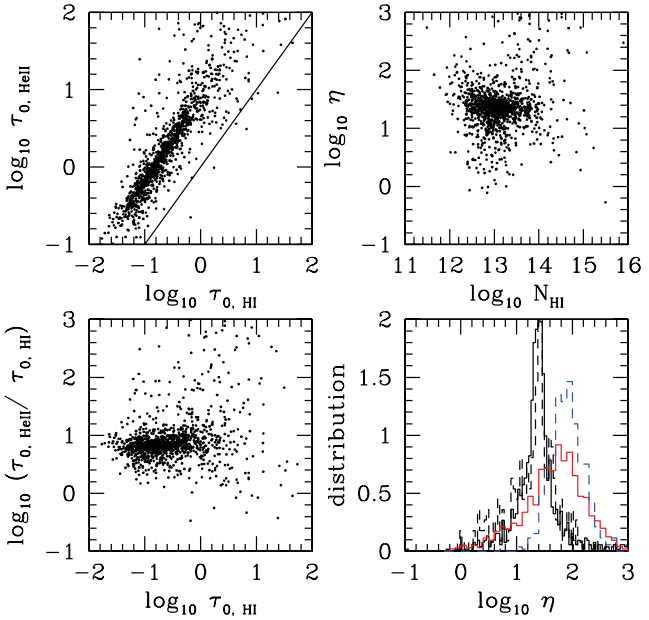

Figure 27. Comparison of EnzoOT results for H I and He II line centre optical depths and column densities for fit absorption features at $z = 2.5$. Top-left panel: comparison of line centre optical depths for H I and He II absorption features. The solid line shows the relation $\tau_{0,\mathrm{He\,II}} = \tau_{0,\mathrm{H\,I}}$. Bottom-left panel: He II to H I line centre optical depth ratio versus H I line centre optical depth. Top-right panel: He II to H I column density ratio η versus H I column density. Bottom-right panel: distribution functions of η for all lines (solid black histogram) and lines restricted to $0.01 < \tau_{0,\mathrm{H\,I}} < 0.1$ (dashed black histogram). Also shown are the distribution functions for HS 1700+6416 (Fechner et al. 2006) for absorption features in the redshift range $2.29 \lesssim z \lesssim 2.75$ for all the lines (solid red histogram) and for lines restricted to $0.01 < \tau_{0,\mathrm{H\,I}} < 0.1$ (blue dashed histogram). All distribution functions are normalized to unit area.

provides an adequate description of the absorption line widths over the full redshift range of interest.

Absorption lines were fitted to the He II spectrum at $z = 2.5$ from the EnzoOT simulation, for which the median Doppler parameter well matched that of the EnzoRT simulation. As for the EnzoRT simulation, the He II spectra were renormalized to the effective optical depth $\tau_{\mathrm{eff}}^{\mathrm{He\,II}} = 0.74$ measured by Fechner et al. (2006) at $z \simeq 2.45$ to facilitate comparison with their data. The He II absorption features were matched to the H I features, requiring a line centre velocity difference smaller than 10 km s^{-1} for a successful match. The relation between the matching line centre optical depths is shown in Fig. 27. The H I and He II line centre optical depths correlate, as in the EnzoRT simulation. The ratio $\tau_{0,\mathrm{He\,II}}/\tau_{0,\mathrm{H\,I}}$, however, is distinctly smaller, about half that found for the EnzoRT simulation. The ratio does not flatten for systems with $\tau_{0,\mathrm{H\,I}} > 1$, contrary to the EnzoRT simulation for which some shadowing of the H I ionization field was present.

Since RT is not included, all the gas is exposed to the same radiation field, so that there should be a unique value for the column density ratio $\eta = N_{\mathrm{He\,II}}/N_{\mathrm{H\,I}}$. The ratio, shown in the right-hand panels of Fig. 27, is indeed more concentrated than in the EnzoRT simulation. The trend of decreasing η with increasing $N_{\mathrm{H\,I}}$ found in the EnzoRT simulation is absent. The distribution of η is much more sharply peaked, with little difference between the full sample and the sample restricted to those systems with $0.01 < \tau_{0,\mathrm{H\,I}} < 0.1$. The peak value of both distributions is at $\eta \simeq 25$, about half the values found for the EnzoRT simulation. The spread in values arises from line deblending by the line-fitting algorithm, which will not always identify identical features in the H I and He II spectra. The tail of low η values, found in the EnzoRT simulation for the sample unrestricted in H I line centre optical depth, is absent.

7 CONCLUSIONS

A RT module based on the method of Tittley & Meiksin (2007) was incorporated into the gravity-hydrodynamics code ENZO to investigate the impact of He II reionization on the structure of the IGM. The RT module is specifically designed to account for the heating by the hardening of the radiation field on passing through inhomogeneities in the density field, crucial for capturing the heating due to hard sources like QSOs. The combined code is able to capture the hydrodynamical feedback following the reionization of both hydrogen and helium.

A simulation of a plane-wave ionization front sweeping across a volume $25\,h^{-1}$ Mpc (comoving) on a side, representing a characteristic ionization front produced by photoionizing sources, was performed. The source spectrum was initially a starburst, transforming gradually into a QSO spectrum $f_\nu \sim \nu^{-0.5}$ over the redshift interval $3 < z < 4$ to represent the onset of He II reionization by QSO sources. Two simulations in the optically thin limit, one without and one with the He II heating rate doubled, and an N-body based pseudo-hydrodynamics simulation with RT using PMRT are performed with identical initial conditions to the EnzoRT simulation in order to examine how well results from these simpler approximate methods compare.

Substantial heating is introduced by He II reionization, with temperatures exceeding those following He II reionization in the optically thin limit by typically 10–20 $\times$ 10^3 K. High temperatures, in excess of 35 $\times$ 10^3 K, are produced in the 'shadows' of overdense structures as the He II is photoionized by a radiation field hardened on passing through the overdense structures. While peculiar velocities are boosted by 0.1–10 km s^{-1} by $z = 3$ over a simulation with no He II reionization, the differences compared with a simulation with He II reionization in the optically thin limit are typically smaller than 1 km s^{-1}. The expansion of the gas following He II reionization, however, plays an important role in curtailing the hardening of the radiation field by reducing the gas density in small haloes. As a result, the temperature–density relation is somewhat tighter and flatter compared with the corresponding PMRT simulation, for which no hydrodynamical response is accounted for. In rare regions, the temperature in dense regions when RT is included is lower than the corresponding ENZO simulation in the optically thin limit, a consequence of complete shadowing of He II ionizing photons by dense clumps in the RT computation. Towards the end of the epoch of He II reionization, the numbers of such regions would be reduced by the overlapping of helium ionization fronts.

The gas flows induced by He II reionization alter the gas density field on large scales (several comoving megaparsecs in extent), with density reductions by as much as 10–20 per cent compared with a simulation without He II reionization. In much smaller regions, the gas is pushed into structures with density increases of up to 50 per cent. Compared with a simulation with He II re-ionized in the optically thin limit, the density changes are much reduced, with large-scale reductions of ∼5 per cent, and density enhancements of a few to several per cent in complex density regions.

Because the dark matter is coupled gravitationally to the gas, displacements in the gas will produce displacements in the dark matter as well. Large-scale coherent reductions in the dark matter

density of up to 0.5 per cent are found at $z = 3$, increasing to nearly 1 per cent by $z = 2$. Small dense regions show enhancements in density by 0.2 per cent at $z = 3$ to 1 per cent at $z = 2$. The dark matter and gas density displacements may produce distortions of a few per cent in the matter power spectrum on comoving wavenumber scales of $k > 0.5\,h\,\mathrm{Mpc}^{-1}$.

The reionization of He II has a substantial impact on the H I Lyα forest, as would be measured in the spectra of background QSOs. Synthetic spectra are drawn from the simulations and normalized according to measured values of the mean H I and He II transmission values. The most conspicuous effect is on the broadening of the absorption features. As the Doppler parameter distribution may be measured to high accuracy in a given QSO spectrum, with a median Doppler parameter determined to a precision of $\sim$1 km s^{-1} or better, the line widths are a potentially powerful means of constraining the He II reionization process and the nature of the ionizing sources. (Alternative measures of the line shapes, such as discrete wavelet coefficients or the flux curvature, may similarly be sensitive probes of the reionization history.) The heating induced by RT, however, will affect the other flux-related statistics as well.

Compared with He II reionization in the optically thin limit, the boost in temperatures when RT is included produces a larger fraction of weak H I absorption features with optical depths <0.1, and a smaller fraction of moderate optical depth systems with optical depths 0.1–0.6. This may be accounted for by the increase in the line widths and reduction in the neutral fraction at a given gas density due to the higher temperatures, as both tend to reduce the line centre optical depth of the absorption features. The modifications to the optical depths result in a shift in the pixel flux cumulative distribution, with a maximum difference between the cumulative distributions from the ENZO runs with and without RT of $\sim$0.1 at $z = 3$, readily detectable in measured spectra.

The H I Lyα forest spectra are found to be fully resolvable into absorption features. The resulting H I column density distribution of the fit lines is somewhat broader when RT is taken into account compared with the optically thin simulation. Fewer narrow lines are found in the simulation with RT than without. The median Doppler parameter evolves little in the range $2.5 \le z \le 3.5$, with $b_{\rm med} \simeq 35\,\mathrm{km\,s^{-1}}$, but decreases to $b_{\rm med} \lesssim 25\,\mathrm{km\,s^{-1}}$ by $z = 2$. Dividing the absorption features into those optically thin and optically thick at line centre reveals a sharp difference in the evolution of the features. Those optically thick evolve slowly, increasing from $b_{\rm med} \simeq 27\,\mathrm{km\,s^{-1}}$ when He II reionization begins at $z = 4.0$ to $b_{\rm med} \simeq 33\,\mathrm{km\,s^{-1}}$ at $z = 3.5$, then gradually diminishing to $b_{\rm med} \simeq 19\,\mathrm{km\,s^{-1}}$ at $z = 2.0$. By contrast, the median Doppler parameter of the optically thin lines increases rapidly from $b_{\rm med} \simeq 21\,\mathrm{km\,s^{-1}}$ at $z = 4.0$ to $b_{\rm med} \simeq 44 - 45\,\mathrm{km\,s^{-1}}$ at $3.0 \le z \le 3.5$, then diminishes slightly to $b_{\rm med} \simeq 39\,\mathrm{km\,s^{-1}}$ at $z = 2.5$ and rapidly to $b_{\rm med} \simeq 27\,\mathrm{km\,s^{-1}}$ by $z = 2.0$. The median Doppler widths of the optically thick systems agree well with those measured. By contrast, the median values of the optically thin systems at $3 < z < 3.5$ substantially exceed those measured, suggesting either He II reionization was imposed too late in the simulation, having just completed at $z \simeq 3$, or that the source spectrum is too hard. A previous PMRT simulation with He II reionization initiated at $z = 5.0$ (Tittley & Meiksin 2007) produced a substantially lower peak temperature of 15×10^3 K by $z = 3.0$, cooler than found here by 10–20$\times 10^3$ K. Cooler temperatures may thus be achieved if He II reionization were substantially completed prior to $z = 3$, although this may be at tension with recent claims that He II reionization extended to $z < 3$. The PMRT simulations also found cooler temperatures arose when a single power-law spectrum re-ionized both hydrogen and helium, so that the temperatures are sensitive to the amount of He II reionization during the hydrogen reionization epoch. Clearly, simulations allowing for a more complex He II reionization history involving a range of source histories and spectra are required to fully match the data.

The PMRT simulation matches the median Doppler width of the optically thick absorbers in the EnzoRT simulation to an accuracy of 2 km s^{-1} at $z \ge 4$ and better than 0.5 km s^{-1} at $2 \le z \le 2.5$, but underpredicts the widths by as much as 3.5 km s^{-1} at intermediate redshifts. For the absorbers optically thin at line centre, the agreement is to better than 2 km s^{-1} for $3.0 \le z \le 5$, but underpredicts the widths by $\sim$5 km s^{-1} by $z = 2.0$.

Doubling the He II heating rate in an optically thin ENZO simulation produces a close match to the median Doppler parameter of the optically thin absorbers from the EnzoRT simulation over $3.0 \le z \le 3.5$, agreeing to within 0.6 km s^{-1}. But by $z = 2.0$, the median Doppler parameter is overpredicted by $\sim$15 km s^{-1}. The Doppler parameters of the absorption systems optically thick at line centre are overpredicted by 2–6 km s^{-1} over $2.0 \le z \le 3.5$. The approximate methods are thus unable to reproduce the correct amount of broadening to the accuracy with which it is measured over the full range of redshifts for which the forest may be observed in high resolution, high signal-to-noise ratio spectra.

Just as absorption features may fully account for the pixel flux distribution in Lyα, a line blanketing model accounts well for the evolution in the mean transparency of the IGM in higher order Lyman series lines. Effective optical depth ratios for the H I of $\tau^{\rm eff}_{{\rm Ly}\beta}/\tau^{\rm eff}_{{\rm Ly}\alpha} \simeq 0.36$ and $\tau^{\rm eff}_{{\rm Ly}\gamma}/\tau^{\rm eff}_{{\rm Ly}\alpha} \simeq 0.21$ are predicted at $z = 3.0$ from the EnzoRT simulation.

RT through density inhomogeneities in the IGM results in a wide spread of He II Lyα optical depths compared with H I even after He II reionization has completed in the simulation at $z = 3$. A broad peak centred at $\tau_{\rm He\,II}/\tau_{\rm H\,I} \simeq 105$ is found at $z = 3.0$, diminishing to 80 at $z = 2.5$ and 75 at $z = 2.0$.

As for the H I, the pixel flux distribution for He II Lyα may be fully accounted for by absorption lines for $2.0 \le z \le 2.5$. At $z = 3.0$, however, the mean transmission is too low for meaningful absorption line fitting to be performed. The He II spectra were renormalized to $\tau^{\rm He\,II}_{\rm eff} = 0.74$ at $z = 2.5$ to compare with the measurements of Fechner et al. (2006). Matching the He II absorption features to the corresponding H I features results in a broad distribution of the column density ratio $\eta = N_{\rm He\,II}/N_{\rm H\,I}$, with a peak of $\eta \simeq 50$, similar to the measured distribution. A comparison with the distribution produced by the EnzoOT simulation, however, shows that much of the width in the distribution is an artefact of the deblending of the absorption features by the line-fitting algorithm.

Comparison between the peak column density and optical depth ratios indicates a typical Doppler parameter ratio of $\xi = b_{\rm He\,II}/b_{\rm H\,I} \simeq 0.9$, close to the velocity-broadened limit of $\xi = 1$. A comparison based on well deblended, unsaturated systems with line centre H I optical depths $0.01 < \tau_0 < 0.1$ shows a range in Doppler parameter ratios peaking in the range $0.5 < \xi < 1.0$, the lower value corresponding to the limit of thermally broadened features.

Line blanketing accounts well for the higher order He II Lyman transmission through the IGM as well. The simulations predict effective optical depth ratios of $\tau^{\rm eff}_{{\rm Ly}\beta}/\tau^{\rm eff}_{{\rm Ly}\alpha} \simeq 0.36$ at $z = 2.5$, in agreement with the measured value, and $\tau^{\rm eff}_{{\rm Ly}\gamma}/\tau^{\rm eff}_{{\rm Ly}\alpha} \simeq 0.20$ (currently unmeasured).

A range of models, allowing for multiple QSO sources turning on over a range of redshifts with a variety of luminosities, spectral shapes and lifetimes, would be required to accurately match the H I and He II absorption data as measured in the spectra of high-redshift background QSOs. The simulations presented here demonstrate that

He II reionization simulations including RT are required to fully exploit the growing body of high-quality IGM data at both optical and UV wavelengths.

ACKNOWLEDGMENTS

The computations reported here were performed using the SUPA Astrophysical HPC facility and facilities funded by an STFC Rolling Grant. ERT is supported by an STFC Rolling Grant. Computations described in this work were performed using the ENZO code developed by the Laboratory for Computational Astrophysics at the University of California in San Diego (http://lca.ucsd.edu).

REFERENCES

Abel T., Norman M. L., Madau P., 1999, ApJ, 523, 66
Anderson S. F., Hogan C. J., Williams B. F., Carswell R. F., 1999, AJ, 117, 56
Becker G. D., Bolton J. S., Haehnelt M. G., Sargent W. L. W., 2011, MNRAS, 410, 1096
Bolton J. S., Becker G. D., 2009, MNRAS, 398, L26
Bolton J. S., Haehnelt M. G., 2007, MNRAS, 374, 493
Bolton J., Meiksin A., White M., 2004, MNRAS, 348, L43
Bolton J. S., Haehnelt M. G., Viel M., Springel V., 2005, MNRAS, 357, 1178
Bolton J. S., Haehnelt M. G., Viel M., Carswell R. F., 2006, MNRAS, 366, 1378
Bryan G. L., Machacek M. E., 2000, ApJ, 534, 57
Bryan G. L., Machacek M., Anninos P., Norman M. L., 1999, ApJ, 517, 13
Burles S., Tytler D., 1997, AJ, 114, 1330
Davé R., Hernquist L., Weinberg D. H., Katz N., 1997, ApJ, 477, 21
Davidsen A. F., Kriss G. A., Zheng W., 1996, Nat, 380, 47
Fardal M. A., Giroux M. L., Shull J. M., 1998, AJ, 115, 2206
Faucher-Giguère C.-A., Prochaska J. X., Lidz A., Hernquist L., Zaldarriaga M., 2008, ApJ, 681, 831
Fechner C. et al., 2006, A&A, 455, 91
Furlanetto S. R., Dixon K. L., 2010, ApJ, 714, 355
Haardt F., Madau P., 1996, ApJ, 461, 20
Heap S. R., Williger G. M., Smette A., Hubeny I., Sahu M. S., Jenkins E. B., Tripp T. M., Winkler J. N., 2000, ApJ, 534, 69
Jakobsen P., Boksenberg A., Deharveng J. M., Greenfield P., Jedrzejewski R., Paresce F., 1994, Nat, 370, 35
Kriss G. A. et al., 2001, Sci, 293, 1112
Larson D. et al., 2011, ApJS, 192, 16
McQuinn M., Lidz A., Zaldarriaga M., Hernquist L., Hopkins P. F., Dutta S., Faucher-Giguère C.-A., 2009, ApJ, 694, 842
Madau P., Meiksin A., 1994, ApJ, 433, L53
Meiksin A., 1994, ApJ, 431, 109
Meiksin A., 2005, MNRAS, 356, 596
Meiksin A. A., 2009, Rev. Modern Phys., 81, 1405
Meiksin A., White M., 2001, MNRAS, 324, 141
Meiksin A., White M., 2003, MNRAS, 342, 1205
Meiksin A., White M., 2004, MNRAS, 350, 1107
Meiksin A., Bryan G., Machacek M., 2001, MNRAS, 327, 296
Meiksin A., Tittley E. R., Brown C. K., 2010, MNRAS, 401, 77
Miralda Escudé J., Rees M. J., 1994, MNRAS, 266, 343
Reimers D., Kohler S., Wisotzki L., Groote D., Rodriguez-Pascual P., Wamsteker W., 1997, A&A, 327, 890
Reimers D., Fechner C., Hagen H.-J., Jakobsen P., Tytler D., Kirkman D., 2005, A&A, 442, 63
Schaye J., Theuns T., Rauch M., Efstathiou G., Sargent W. L. W., 2000, MNRAS, 318, 817
Scott J. E., Kriss G. A., Brotherton M., Green R. F., Hutchings J., Shull J. M., Zheng W., 2004, ApJ, 615, 135
Shull J. M., Tumlinson J., Giroux M. L., Kriss G. A., Reimers D., 2004, ApJ, 600, 570
Shull J. M., France K., Danforth C. W., Smith B., Tumlinson J., 2010, ApJ, 722, 1312
Smette A., Heap S. R., Williger G. M., Tripp T. M., Jenkins E. B., Songaila A., 2002, ApJ, 564, 542
Steigman G., 2007, Annu. Rev. Nuclear Particle Sci., 57, 463
Syphers D., Anderson S. F., Zheng W., Meiksin A., Haggard D., Schneider D. P., York D. G., 2011a, ApJ, 726, 111
Syphers D. et al., 2011b, ApJ, 742, 99
Telfer R. C., Zheng W., Kriss G. A., Davidsen A. F., 2002, ApJ, 565, 773
Theuns T., Leonard A., Efstathiou G., Pearce F. R., Thomas P. A., 1998, MNRAS, 301, 478
Theuns T., Schaye J., Haehnelt M. G., 2000, MNRAS, 315, 600
Tittley E. R., Meiksin A., 2007, MNRAS, 380, 1369
Tytler D., Paschos P., Kirkman D., Norman M. L., Jena T., 2009, MNRAS, 393, 723
Wolf C., Wisotzki L., Borch A., Dye S., Kleinheinrich M., Meisenheimer K., 2003, A&A, 408, 499
Worseck G. et al., 2011, ApJ, 733, L24
Zheng W., Chiu K., Anderson S. F., Schneider D. P., Hogan C. J., York D. G., Burles S., Brinkmann J., 2004a, AJ, 127, 656
Zheng W. et al., 2004b, ApJ, 605, 631
Zheng W. et al., 2008, ApJ, 686, 195
Zuo L., 1992, MNRAS, 258, 36

This paper has been typeset from a TEX/LATEX file prepared by the author.